

Resilience through diversity: Loss of neuronal heterogeneity in epileptogenic human tissue impairs network resilience to sudden changes in synchrony

Scott Rich^{1,*}, Homeira Moradi Chameh¹, Jeremie Lefebvre^{1,2,3,†}, and Taufik A Valiante^{1,4,5,6,7,†}

¹Krembil Research Institute, University Health Network (UHN), Division of Clinical and Computational Neuroscience, Toronto, Ontario, Canada

²University of Ottawa, Department of Biology, Ottawa, Ontario, Canada

³University of Toronto, Department of Mathematics, Toronto, Ontario, Canada

⁴University of Toronto, Institute of Biomedical Engineering, Toronto, ON, Canada

⁵University of Toronto, Electrical and Computer Engineering, Toronto, ON, Canada

⁶University of Toronto, Institute of Medical Science, Toronto, ON, Canada

⁷University of Toronto, Division of Neurosurgery, Department of Surgery, Toronto, ON, Canada

*Corresponding Author: scott.rich@uhnresearch.ca

†These authors share senior authorship of this work.

October 19, 2021

Abstract

A myriad of pathological changes associated with epilepsy can be recast as decreases in cell and circuit heterogeneity. We thus propose recontextualizing epileptogenesis as a process where reduction in cellular heterogeneity renders neural circuits less resilient to seizure. By comparing patch clamp recordings from human layer 5 (L5) cortical pyramidal neurons from epileptogenic and non-epileptogenic tissue, we demonstrate significantly decreased biophysical heterogeneity in seizure generating areas. Implemented computationally, this decreased heterogeneity renders model neural circuits prone to sudden transitions into synchronous states with increased firing activity, paralleling ictogenesis. This computational work also explains the surprising finding of significantly decreased excitability in the population activation functions of neurons from epileptogenic tissue. Finally, mathematical analyses reveal a unique bifurcation structure arising only with low heterogeneity and associated with seizure-like dynamics. Taken together, this work provides experimental, computational, and mathematical support for the theory that ictogenic dynamics accompany a reduction in biophysical heterogeneity.

Keywords— Epilepsy | Seizure | Neuronal heterogeneity | Computational neuroscience | Neuronal electrophysiology

Introduction

Epilepsy, the most common serious neurological disorder in the world (Reynolds, 2002), is characterized by the brain’s proclivity for seizures, which exhibit highly correlated electrophysiological activity and elevated neuronal spiking (Jiruska et al., 2013). While the etiologies that predispose the brain to epilepsy are myriad (Jasper, 2012), the dynamics appear to be relatively conserved (Jirsa et al., 2014; Saggio et al., 2020), suggesting a small palette of candidate routes to the seizure state. One potential route to ictogenesis is disruption of excitatory/inhibitory balance (EIB) - a possible “final common pathway” for various epileptogenic etiologies motivating decades of research into epilepto- and ictogenesis (Dehghani et al., 2016; Žiburkus et al., 2013). A disrupted EIB can impair the resilience of neural circuits to correlated inputs (Renart et al., 2010), a paramount characteristic of ictogenesis. In addition to EIB, biophysical heterogeneity also provides resilience to correlated inputs (Mishra & Narayanan, 2019). Thus, EIB can be considered a synaptic mechanism for input decorrelation, while biophysical heterogeneity contributes to decorrelation post-synaptically.

Cellular heterogeneity is the norm in biological systems (Altschuler & Wu, 2010; Marder & Goaillard, 2006). In the brain, experimental and theoretical work has demonstrated that such heterogeneity expands the informational content of neural circuits, in part by reducing correlated neuronal activity (Padmanabhan & Urban, 2010; Tripathy et al., 2013). Since heightened levels of firing and firing rate correlations hallmark seizures (Jirsa et al., 2014; Zhang et al., 2011), we hypothesize that epilepsy may be likened, in part, to

33 pathological reductions in biological heterogeneity which impair decorrelation, and thus circuit resilience
34 to information poor (Trevelyan et al., 2013), high-firing (Jiruska et al., 2013), and highly-correlated states
35 (Zhang et al., 2011).

36 A number of pathological changes accompanying epileptogenesis can be recast as decreases in biological
37 heterogeneity. Losses of specific cell-types homogenize neural populations (Cossart et al., 2001; Cobos et al.,
38 2005), down- or upregulation of ion channels homogenize biophysical properties (Arnold et al., 2019; Klaassen
39 et al., 2006; Albertson et al., 2011), and synaptic sprouting homogenizes neural inputs (Sutula & Dudek,
40 2007). This recontextualizes epileptogenesis as a process associated with the progressive loss of biophysical
41 heterogeneity.

42 To explore this hypothesis we combine electrophysiological recordings from human cortical tissue, compu-
43 tational modeling, and mathematical analysis to detail the existence and consequences of one reduction in
44 biological heterogeneity in epilepsy: the decrease of intrinsic neuronal heterogeneity. We first provide experi-
45 mental evidence for decreased biophysical heterogeneity in neurons within brain regions that generate seizures
46 (epileptogenic zone) when compared to non-epileptogenic regions. This data constrains an exploration of the
47 effects of heterogeneity in neural excitability on simulated brain circuits. Using a cortical excitatory-inhibitory
48 (E-I) spiking neural network, we show that networks with neuronal heterogeneity mirroring epileptogenic
49 tissue are more vulnerable to sudden shifts from an asynchronous to a synchronous state with clear parallels
50 to seizure onset. Networks with neuronal heterogeneity mirroring non-epileptogenic tissue are more resilient
51 to such transitions. These differing heterogeneity levels also underlie significant, yet counter-intuitive, differ-
52 ences in neural activation functions (i.e., frequency-current or FI curves) measured inside and outside the
53 epileptogenic zone. Using mean-field analysis, we show that differences in the vulnerability to these sudden
54 transitions and activation functions are both consequences of varying neuronal heterogeneities. Viewed
55 together, our experimental, computational, and mathematical results strongly support the hypothesis that
56 biophysical heterogeneity enhances the dynamical resilience of neural networks while explaining how reduced
57 diversity can predispose circuits to seizure-like dynamics.

58 **Results**

59 **Intrinsic biophysical heterogeneity is reduced in human epileptogenic cortex**

60 In search of experimental evidence for reduced biophysical heterogeneity in epileptogenic regions, we utilized
61 the rare access to live human cortical tissue obtained during resective surgery. Whole-cell current clamp
62 recordings characterized the passive and active properties of layer 5 (L5) cortical pyramidal cells from these

63 samples, a cell type we have shown to display notable biophysical heterogeneity (Moradi Chameh et al.,
64 2021). Biophysical properties of neurons from epileptogenic frontal lobe cortex were contrasted to frontal lobe
65 neurons of patients with no previous history of seizures undergoing tumor resection. Additionally, we obtained
66 recordings from neurons in non-epileptogenic middle temporal gyrus (MTG) from patients with mesial
67 temporal sclerosis, which is the overlying cortex routinely removed to approach deep temporal structures.
68 The MTG is a well-characterized part of the human brain, representing a common anatomical region from
69 which non-epileptogenic brain tissue has been studied electrophysiologically and transcriptomically (Hodge
70 et al., 2019; Moradi Chameh et al., 2021; Beaulieu-Laroche et al., 2018; Kalmbach et al., 2021), and thus our
71 primary source of non-epileptogenic neurons. We note that each of these studies classify these neurons as
72 indicative of “seemingly normal” human neurons independent of the patients’ epilepsy diagnoses (i.e., a best
73 case control given limitations in obtaining human tissue).

74 Our analysis concentrated on two characterizations of cellular excitability. The first was the distance to
75 threshold (DTT) measured as the difference between the resting membrane potential (RMP) and threshold
76 voltage (see Supplementary Figure S1 for these and other electrophysiological details). Whole-cell recordings
77 revealed less DTT variability (smaller coefficient of variation (CV); $p=0.04$; two sample coefficient of variation
78 test) in neurons from epileptogenic frontal lobe ($n=13$, $CV=20.3\%$) as compared to non-epileptogenic MTG
79 ($n=77$, $CV=37.1\%$). A significant difference (smaller CV; $p=0.03$) was also seen when comparing epileptogenic
80 frontal lobe to non-epileptogenic frontal lobe ($n=12$, $CV=40.8\%$). Meanwhile, the CVs were not significantly
81 different when comparing non-epileptogenic MTG and non-epileptogenic frontal lobe ($p=0.7$). These features
82 are more easily appreciated from the Gaussian fits of this data presented in Figure 1(b); all three data sets
83 were deemed normal after passing both the Shapiro-Wilk and D’Agostino & Pearson omnibus normality tests
84 with $\alpha=0.05$. These results imply that the decrease in biophysical heterogeneity observed in epileptogenic
85 cortex was not confounded by sampling from the temporal versus frontal lobe.

86 While our non-epileptogenic MTG population is larger, this is unavoidable given the availability of human
87 cortical tissue and the additional efforts required to confirm the tissue’s epileptogenic nature (see Discussion).
88 Statistical tests accounting for unequal population sizes were used. Additionally, the significant difference
89 between the standard deviations (SDs) of the DTTs in non-epileptogenic MTG and epileptogenic frontal
90 lobe ($p=0.03$, Cohen’s d effect size= 0.5 ; F-test; $SD=7.8$ mV in non-epileptogenic MTG and $SD=4.4$ mV in
91 epileptogenic frontal lobe) that is implemented in our models has a “moderate” effect size.

92 Our second quantification of cellular excitability was the FI curve (i.e., activation function), which captures
93 the firing rate (F) as function of input current (I). The activation function of the population of neurons
94 from the epileptogenic zone displayed qualitative and quantitative differences compared to neurons from
95 both non-epileptogenic MTG and frontal lobe (Figure 1(c)). Surprisingly, firing threshold was higher in

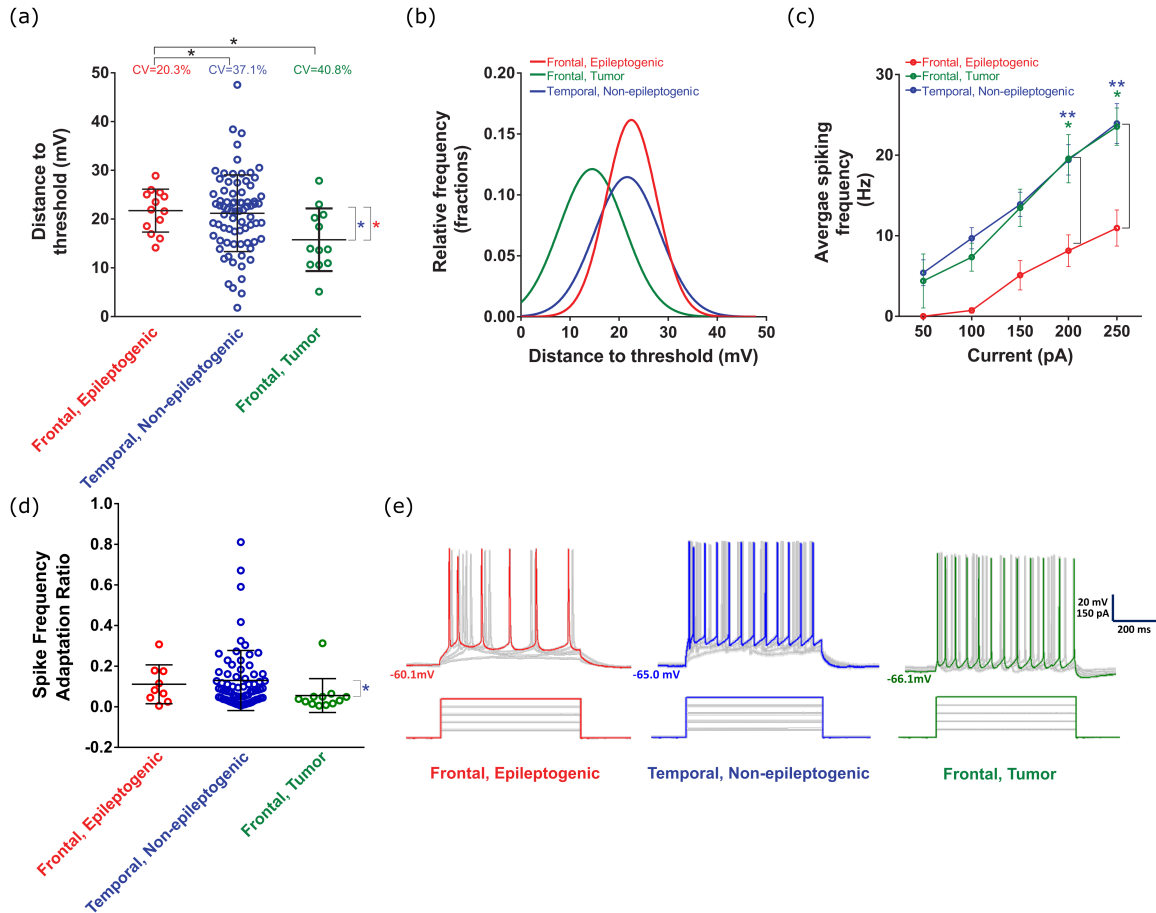


Figure 1. *In vitro* human tissue recordings reveal significantly different electrophysiological heterogeneity between epileptogenic and non-epileptogenic populations. (a): The coefficient of variation (CV) in the distance to threshold (DTT) is significantly larger in both the temporal, non-epileptogenic (i.e., non-epileptogenic MTG; n=77) and frontal, tumor (i.e., non-epileptogenic frontal lobe; n=12) populations compared to the frontal, epileptogenic (i.e., epileptogenic frontal lobe; n=13) population ($p=0.04$ to temporal, non-epileptogenic, $p=0.03$ to frontal, tumor; two sample coefficient of variation test). The CV measure is implemented considering the significantly reduced mean DTT in frontal, tumor data compared to the other two populations ($p=0.01$ for both comparisons; non-parametric Mann-Whitney test). We compare the frontal, epileptogenic and temporal, non-epileptogenic populations computationally given their similar mean DTT ($p=0.7$). Plotted bars indicate mean \pm standard deviation (SD). (b): An alternative visualization of the DTT distributions via fit Gaussian probability density functions. All three data sets were deemed normal after passing both the Shapiro-Wilk and D’Agostino & Pearson omnibus normality test with $\alpha=0.05$. (c): Neurons from non-epileptogenic populations show similar, linear activation functions (i.e., FI curves). Firing frequency is significantly lower in the frontal, epileptogenic population for a 200 pA injection compared to the temporal, non-epileptogenic ($p=0.009$; two-way ANOVA-Tukey’s multiple comparison test) and frontal, tumor ($p=0.03$) populations, as well as for a 250 pA injection compared to the temporal, non-epileptogenic ($p=0.002$) and frontal, tumor ($p=0.02$) populations. Plotted bars indicate mean \pm standard error measure (SEM). (d): All three populations show a similar spike frequency adaptation ratio (see details in Methods), with the only significant difference being between the means from the frontal, tumor and temporal, non-epileptogenic populations ($p=0.01$; One-Way ANOVA post hoc with Dunn’s multiple comparison test). Plotted bars indicate mean \pm SD. (e): Example cell voltage responses following depolarizing current injections (50-250 pA) from all three populations, as used to calculate the FI curve (colors denote population as in previous panels).

96 the epileptogenic zone compared to both non-epileptogenic populations. Additionally, firing rates were
 97 significantly lower in the epileptogenic zone ($p=0.03$ when comparing to non-epileptogenic frontal lobe at

98 200 pA, $p=0.02$ when comparing to non-epileptogenic frontal lobe at 250 pA, $p=0.009$ when comparing
99 to non-epileptogenic MTG at 200 pA, and $p=0.002$ when comparing to non-epileptogenic MTG at 250
100 pA; two-way ANOVA-Tukey's multiple comparison test), indicating larger inputs are required to induce
101 high-frequency repetitive firing in individual neurons from epileptogenic tissue. This non-linear behavior is in
102 strong contrast to the activation functions measured in non-epileptogenic zones, characterized by both higher
103 and more linear changes in firing rates. All three populations show a similar spike frequency adaptation ratio
104 (Figure 1(d)), including no significant difference between epileptogenic frontal lobe and non-epileptogenic
105 MTG (the regions focused on in our modeling), indicating that differences in the FI curve are not due to
106 differing adaptation rates. Example firing traces from each population (in response to each of the current steps
107 used in FI curve generation; note that the spike frequency adaptation ratio is calculated from *one* of these
108 steps, chosen as described in the Methods for each individual neuron) are found in Figure 1(e). This increased
109 excitability of the non-epileptogenic populations appears contradictory to the understanding of seizure as a
110 hyperactive brain state, although some prior studies have hinted at this phenomenon (Colder et al., 1996;
111 Schwartzkroin et al., 1983); additionally, the significantly increased first-spike latency in our epileptogenic
112 population (see Supplementary Figure S1(c)) is additional evidence for the decreased single-cell excitability
113 of neurons in this population. We further investigate this in the context of biophysical heterogeneity below.

114 **Spiking E-I neural networks with epileptogenic levels of excitatory heterogeneity** 115 **are more vulnerable to sudden changes in synchrony**

116 Given these confirmatory experimental results, we next explored the effects of biophysical heterogeneity on
117 the transition to a synchronous state akin to the transition to seizure (Zhang et al., 2011). We developed a
118 spiking network model of a cortical microcircuit comprised of recurrently connected excitatory and inhibitory
119 neurons (see details in Methods), motivated in part by the long history of seizure modeling (Kramer et al.,
120 2005; Jirsa et al., 2014) and previous models of decorrelated activity in the cortex (Vogels & Abbott, 2009;
121 Renart et al., 2010; Ostojic, 2014). Our choice of model parameters (see details in Methods) positioned the
122 system near a tipping point at which synchronous activity might arise (Jadi & Sejnowski, 2014a,b; Neske
123 et al., 2015; Rich et al., 2020b) in order to determine the effects of cellular heterogeneity on this potential
124 transition.

125 We subjected these networks to a slowly linearly increasing external drive to the excitatory cells. This
126 allowed us to observe the dynamics and stability of the asynchronous state, known to be the physiological
127 state of the cortex (Vogels & Abbott, 2009; Renart et al., 2010; Ostojic, 2014), by determining how vulnerable
128 the network is to a bifurcation forcing the system into a state of increased synchrony and firing. A biological

129 analogue for this paradigm would be an examination of whether induced hyper-excitability might drive the
130 onset of seizure-like activity *in vitro*, although such perturbations can more easily be performed continuously
131 (i.e., our linearly increasing external drive) *in silico*.

132 To facilitate implementing experimentally-derived heterogeneities in our model, we compared epileptogenic
133 frontal lobe with non-epileptogenic MTG given their similar mean DTT values ($p=0.7$, non-parametric
134 Mann-Whitney test; mean=21.2 mV for non-epileptogenic MTG and mean=21.7 mV for epileptogenic frontal
135 lobe). These populations display significantly different SDs in their DTT values (reported above). Given the
136 definition of our neuron model (rheobases sampled from a normal distribution with with mean 0, see details
137 in Methods), we implement differing heterogeneities by sampling rheobase values for our neural populations
138 from Gaussian distributions with these varying SDs. In this model, the term rheobase refers to the inflexion
139 point of the model neuron activation function (see Methods). Heterogeneity in this mathematically-defined
140 rheobase is the *in silico* analogue of heterogeneity in the DTT (i.e., the distribution of rheobases in Figure
141 2(c-d) corresponds to a horizontal shift to a mean of 0 of the DTT distributions in Figure 1(b)).

142 The rheobase heterogeneity was parameterized by the SD σ_e for excitatory neurons and σ_i for inhibitory
143 neurons (see diagrams in Figure 2(a-b)). This results in diversity in the neurons' activation functions and
144 aligns the variability in their excitabilities with that measured experimentally. We refer to such rheobase
145 heterogeneity simply as heterogeneity in the remainder of the text. Models with epileptogenic (high $\sigma_e = 7.8$
146 mV, Figure 2(e)) and non-epileptogenic (low $\sigma_e = 4.4$ mV, Figure 2(f)) excitatory heterogeneity with
147 identical, moderate inhibitory heterogeneity ($\sigma_i = 10.0$ mV) exhibit distinct behaviors. With low excitatory
148 heterogeneity, a sharp increase in excitatory synchrony associated with increased firing rates is observed. In
149 contrast, when the excitatory heterogeneity was high, both synchrony and firing rates scaled linearly with
150 input amplitude.

151 We further investigated the respective roles of excitatory versus inhibitory heterogeneity in these sudden
152 transitions. With non-epileptogenic excitatory heterogeneity (high σ_e), increases in excitatory synchrony,
153 excitatory firing rates, and inhibitory firing rates were all largely linear regardless of whether σ_i was low
154 (Figure 3(a)) or high (Figure 3(b)). Conversely, with excitatory heterogeneity reflective of epileptogenic
155 cortex (low σ_e), synchronous transitions were observed for both low (Figure 3(c)) and high (Figure 3(d))
156 levels of σ_i . This transition is of notably higher amplitude when σ_i is low, indicative of differing underlying
157 dynamical structures.

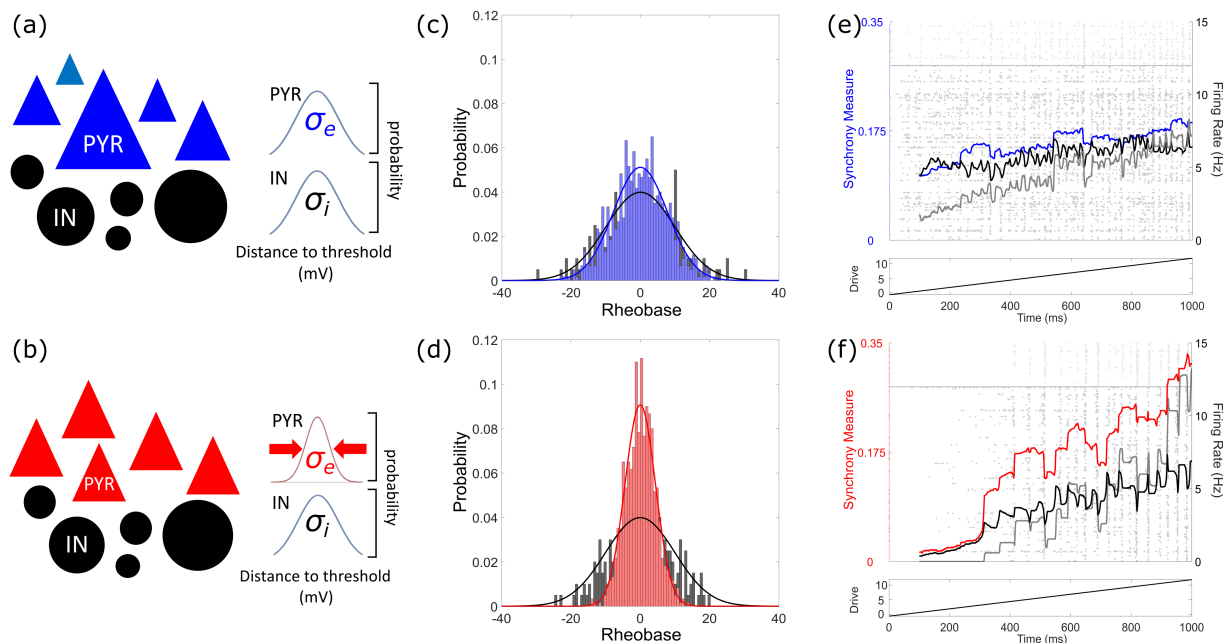


Figure 2. Experimentally observed decreases in heterogeneity amongst excitatory cells promote ictogenic-like transitions in E-I spiking neural network models. (a-b): Schematic representation of model spiking E-I networks, with pyramidal neurons represented as triangles and interneurons as circles. Blue neurons represent non-epileptogenic (i.e. high) levels of heterogeneity (see also the variable neuron sizes) while red neurons represent epileptogenic (i.e. low) levels of heterogeneity (see also the similar neuron sizes). This color schema is maintained in the remaining figures. Here, the inhibitory (black neurons) heterogeneity is set at a moderate value amongst the range studied ($\sigma_i = 10.0$ mV), while $\sigma_e = 7.8$ mV in panel (a) and $\sigma_e = 4.4$ mV in panel (b). **(c-d):** Visualizations of the distribution of model rheobases, with the solid curve (red or blue for excitatory neurons, black for inhibitory neurons) illustrating the Gaussian function and the corresponding histogram illustrating the example random distribution underlying the simulations in this figure. **(e-f):** Example simulations with a linearly increasing excitatory drive. Background: raster plot of network activity, with each circle representing the firing of an action potential of the associated neuron (excitatory neurons below horizontal line, inhibitory neurons above). Foreground: quantifications of network activity taken over 100 ms sliding time windows, with the excitatory synchrony quantified by the Synchrony Measure in blue or red (left axis), as well as excitatory (black) and inhibitory (grey) population firing rates (right axis). Bottom: drive ($I(t)$) to the excitatory population.

158 **Dynamical differences in networks with varying levels of heterogeneity are ex-**
 159 **plained by their distinct mathematical structures**

160 To gain deeper insight into the effect of heterogeneity at a potential transition to synchrony, we derived
 161 and analyzed mathematically the mean-field equations associated with our network model (see Methods).
 162 Specifically, we calculated and classified the fixed points of mean-field equations for different values of σ_e
 163 and σ_i for the range of drives studied in the spiking networks. The fixed point(s) of the mean-field (for
 164 the excitatory population activity, U_e) are plotted in the second row of each panel in Figure 4. These
 165 values correspond to population averages of the (unitless) membrane potential analogue taken across the
 166 individual units in our spiking networks (u_j). We then performed linear stability analysis for those fixed
 167 points, extracting eigenvalues which determine the fixed points' stability, and how it might change as input

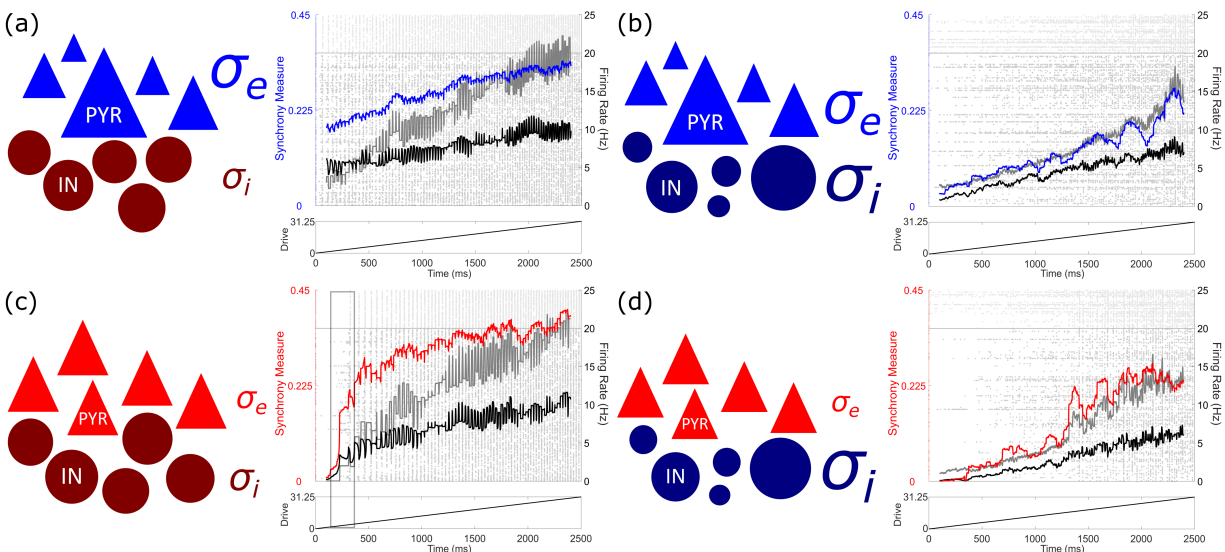


Figure 3. Effects of varied inhibitory heterogeneity on sudden transitions into synchrony in E-I spiking neural network models. Schematics and single simulation visualizations following the conventions of Figure 2 (with inhibitory heterogeneity reflected by darker shaded blue and red neurons), now shown for four combinations of excitatory and inhibitory heterogeneities: $\sigma_e = 7.8$ mV and $\sigma_i = 2.5$ mV in panel (a), $\sigma_e = 7.8$ mV and $\sigma_i = 16.75$ mV in panel (b), $\sigma_e = 4.4$ mV and $\sigma_i = 2.5$ mV in panel (c), and $\sigma_e = 4.4$ mV and $\sigma_i = 16.75$ mV in panel (d). Relative sizes of σ_e and σ_i represent the relative heterogeneity levels. Transitions into high levels of excitatory synchrony are seen in panel (c) and (d), with the transition in panel (c) yielding a notably higher level of synchrony (highlighted by the grey box) and occurring much more abruptly. Meanwhile, changes in the dynamics of panels (a) and (b) are largely linear, with the excitatory synchrony consistently lower when both excitatory and inhibitory heterogeneities are at their highest in panel (b).

168 drive is varied. The dampening rate represents the speed at which the system is either repelled from or returns
 169 to its fixed point(s) and thus classifies their stability (i.e., the real components of eigenvalues associated with
 170 each fixed point). The dampening rate is plotted in the row below the fixed points, followed by the frequency
 171 associated with fixed points with imaginary eigenvalues (i.e., the imaginary components of the eigenvalues).

172 These mean-field analyses confirm that both excitatory and inhibitory heterogeneity have notable impacts
 173 on changes in network dynamics analogous to seizure-onset. In the top row of each panel in Figure 4 we
 174 present quantifications of our spiking network dynamics as in Figure 3, but averaged over 100 independent
 175 simulations. In the presence of high heterogeneity (whenever σ_e and/or σ_i are large, i.e., Figure 4(a), (b),
 176 and (d)), increased drive results in a smooth and approximately linear increase in both mean activity and
 177 synchrony. The mean-field analyses of the associated systems reveal a single fixed point, whose value increases
 178 monotonically with drive. Oscillation frequency is low, indicative of slow-wave activity.

179 The subtle differences in the spiking network dynamics in these scenarios are reflected in differences in the
 180 mean-field analyses. In Figure 4(d) a supercritical Hopf bifurcation (Chow & Hale, 2012) at a high level of
 181 drive (the stable fixed point becomes unstable, giving rise to a stable limit cycle) is associated with a steeper
 182 increase in synchrony. The reverse bifurcation is observed in Figure 4(a) (the unstable fixed point becomes

183 stable) and is associated with a slower increase in synchrony, with the synchrony levels being preserved
184 following this bifurcation due to the noise in the spiking networks allowing for the presence of quasi-cycles
185 (Boland et al., 2008). Meanwhile, the fixed point in Figure 4**(b)** is always stable, reflective of the more
186 constant but shallow increase in synchrony in the spiking network.

187 In contrast to these cases, spiking networks with low heterogeneity (low σ_e and σ_i , Figure 4**(c)**) exhibit
188 sudden increases in mean activity and synchrony. The associated mean-field system displays multistability: it
189 possesses multiple fixed points. As the input drive increases, two of these fixed points coalesce and disappear
190 via a saddle-node bifurcation (Chow & Hale, 2012). The system’s mean activity is thus suddenly drawn
191 towards a preexisting large-amplitude limit cycle. This transition occurs at a drive corresponding with the
192 sudden increase in synchrony and mean activity seen in the spiking network. In the mean-field system, the
193 frequency of resulting oscillations are faster compared to the high heterogeneity scenarios, further emphasizing
194 the uniqueness of the dynamical system with low heterogeneity.

195 We note that the more notable inter-trial variability in Figure 4**(d)** (as illustrated by the fainter \pm SD
196 curves) results from the variable (yet gradual) onset of increased synchrony, in contrast to the transition in
197 Figure 4**(c)** which reliably occurs at a specific drive. The different timings of the onset of synchrony in each
198 independent simulation yield oscillations at different relative phases, which explains why oscillations are not
199 observed in our averaged firing rate measures displayed in Figure 4 (notably, such oscillations are subtle even
200 in the single simulation visualizations of Figure 3 given the 100 ms sliding time window); rather, the presence
201 of oscillatory activity is demarcated by a notable increase in the mean Synchrony Measure.

202 We also emphasize that, in our mathematical analyses, we focus on characterizing the system’s fixed
203 points and inferring from them the presence of oscillatory behavior associated with limit cycles. Directly
204 identifying such limit cycles is a mathematically arduous process (Savov & Todorov, 2000) unnecessary for
205 these analyses, where our primary interest is differentiating the mathematical structure of these four exemplar
206 networks. However, considering the behavior of our spiking networks remains “bounded” (i.e., consistent
207 oscillatory activity is associated with unstable fixed points with imaginary eigenvalues; see Supplementary
208 Figure S2**(b)**), we can confidently infer that such limit cycles exist, as is typical when a bifurcation yields an
209 unstable fixed point.

210 To facilitate the comparison of our spiking networks with our mean-field calculations, we developed a
211 Bifurcation Measure (see Methods) quantifying the tendency for sudden (but persistent) changes in the
212 activity of the spiking network. Higher values of this measure indicate the presence of a more abrupt increase
213 in the quantification of interest as the drive increases. Given the more subtle qualitative difference in the
214 firing rates in our spiking networks, we applied the Bifurcation Measure to the excitatory firing rate (B_e) for
215 the four combinations of σ_e and σ_i examined in Figure 4. This revealed more sudden changes with low σ_e and

216 σ_i ($B_e=0.1050$) as opposed to any other scenario (high σ_e , low σ_i , $B_e=0.0416$; high σ_e , high σ_i , $B_e=0.0148$;
217 low σ_e , high σ_i , $B_e=0.0333$) where the transition is smoother. This analysis indicates that the dynamical
218 transition present in Figure 4(c) is not only unique in the magnitude of the synchronous onset, but also in
219 an associated sudden increase in firing rates.

220 Since the seizure state is typified both by increased synchrony and firing rates (Jiruska et al., 2013; Zhang
221 et al., 2011), this analysis confirms that the sharp transition in these quantities only observed in spiking
222 models with low heterogeneity is driven by a saddle-node bifurcation (Figure 4(c)). These results echo other
223 seizure modeling studies showcasing that ictogenic transitions can arise driven by mathematical bifurcations,
224 and specifically the observation that saddle-node bifurcations underlie abrupt seizure-onset dynamics (Kramer
225 et al., 2005; Jirsa et al., 2014; Saggio et al., 2020). As a corollary, high heterogeneity improves network
226 resilience to sudden changes in synchrony by preventing multistability and fostering gradual changes in
227 network firing rate and oscillatory behavior.

228 **Asymmetric effects of excitatory and inhibitory heterogeneity**

229 Figure 4 highlights distinct effects of excitatory versus inhibitory heterogeneity on the onset of synchrony
230 in spiking networks and the structure of mean-field systems (see the differences between Figure 4(a) and
231 (c)). To clarify these effects we explored a larger parameter space of σ_e and σ_i , as shown in Supplementary
232 Figure S2. For each heterogeneity combination we applied the Bifurcation Measure to excitatory synchrony
233 (B , hereafter referred to simply as the Bifurcation Measure; see details in Methods), which quantifies the
234 abruptness of increased network synchrony in response to a changing network drive. This exploration confirms
235 the asymmetric effect of excitatory and inhibitory heterogeneity on these sudden transitions, with a moderate
236 value of B for low σ_e and high σ_i but a minimal value of B for high σ_e and low σ_i , comporting with patterns
237 observed in previous computational literature (Mejias & Longtin, 2014).

238 Similar asymmetry is seen in our spiking network dynamics (B in Supplementary Figure S2(a) and the
239 Synchrony Measure S in Supplementary Figure S2(b)) and our mean-field systems (the bolded regimes of
240 networks exhibiting multi-stability in Supplementary Figure S2(a) networks exhibiting an unstable fixed
241 point in Supplementary Figure S2(b)). We show an example visualization of the fixed points and their
242 classifications in Supplementary Figure S3. Supplementary Figure S4 shows the details of the determination
243 of fixed point stability in Supplementary Figure S2(b).

244 We further used the Bifurcation Measure to test whether the asymmetric effects of excitatory and inhibitory
245 heterogeneity are generalizable and confirm our system's robustness. In Supplementary Figure S5 we show
246 the pattern followed by B is robust to changes in connectivity density. In the four exemplar cases highlighted

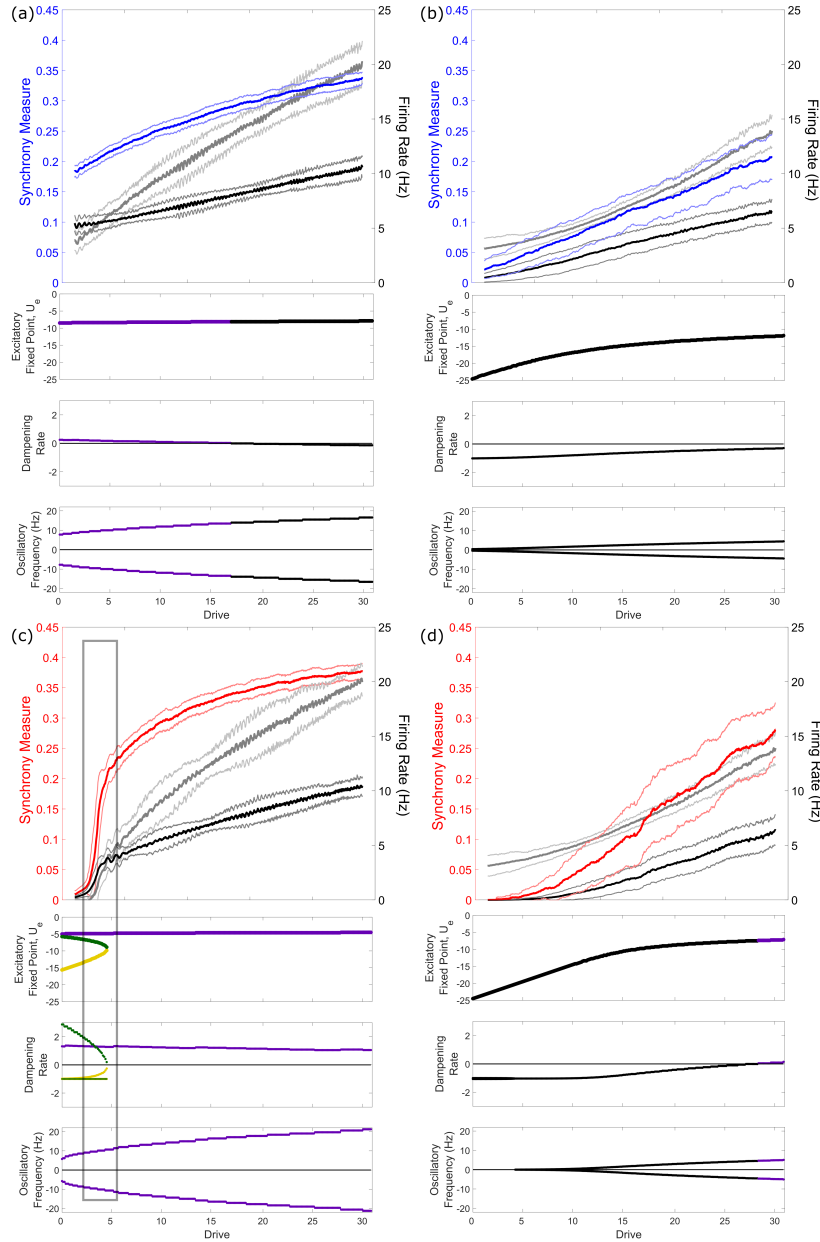


Figure 4. Effects of heterogeneity on spiking network dynamics is explained by stability analysis of mean-field equations. Panels correspond to heterogeneity levels studied in Figure 3. Top row: measures of spiking network dynamics (as seen in Figures 2 and 3) averaged over 100 simulations (dark curve=mean, lighter curve= \pm one SD). Remaining rows: results of stability analysis on mean-field equations corresponding with these networks visualized via the fixed point of mean excitatory activity (top), and the dampening rate and oscillatory frequency associated with each fixed point. Green and gold coloring are used to differentiate the three distinct fixed points in panel c, while the stability of fixed points is color coded (purple=unstable, i.e., positive dampening rate; black=stable, i.e., negative dampening rate). Notably, only in panel (c), where both heterogeneity levels are low, do we see multiple fixed points and a saddle-node bifurcation that occurs at a value of the drive corresponding with the sudden transition in spiking networks (highlighted by the grey box).

247 in Figures 3 and 4 the dynamics are robust for reasonable changes to the primary parameters dictating our
 248 network topology, as shown in Supplementary Figure S6, and similar robustness in the bifurcation structure

249 of the associated mean-field systems is shown in Supplementary Figure S7.

250 This analysis shows that notable decreases in B occur at higher values of σ_i than they do for σ_e , a result
251 which has important implications for our understanding of the potentially differing roles of excitatory and
252 inhibitory heterogeneity in seizure resilience (see Discussion).

253 **Differences in population averaged activation functions explained by differences** 254 **in neuronal heterogeneity**

255 Finally, we return to the counter-intuitive differences in activation functions measured experimentally. As
256 noted previously, the population of neurons from epileptogenic tissue exhibited qualitatively and quantitatively
257 different activation functions via non-linear and hypo-active firing responses (Figure 1(c)).

258 To understand if heterogeneity accounts for these observations, we computed analytically the averaged
259 activation functions of the excitatory populations in our model networks. In Figure 5(a), the experimentally
260 derived firing frequencies from epileptogenic frontal lobe and non-epileptogenic MTG are plotted alongside
261 activation functions of our model populations. For low heterogeneity, the model population's activation
262 function captured both the non-linear and low firing rate responses measured experimentally for neurons
263 in the epileptogenic zone. The increased excitability and linearity seen experimentally in non-epileptogenic
264 tissue was captured by the averaged activation function for our more heterogeneous model population. This
265 comparison is appropriate considering the FI curve data from Figure 1(c) is averaged over the populations of
266 interest, and is thus analogous to the population activation function of our model neurons.

267 To quantitatively support this correspondence, we found the values of σ_e that best fit our experimental
268 data using a non-linear least squares method (see details in Methods). The data from epileptogenic frontal
269 lobe was best fit by an activation function (see Equation 12) with $\sigma_e = 5.0$ mV ($r^2=0.94$), while the data
270 from non-epileptogenic MTG was best fit by an activation function with $\sigma_e = 7.8$ mV ($r^2=0.98$). That the
271 best-fit values closely match the experimentally-observed heterogeneity values means the features of our
272 epileptogenic (resp. non-epileptogenic) activation curves are captured by neural populations with low (resp.
273 high) heterogeneity.

274 This somewhat counter-intuitive result is explained by the linearizing effect that increased heterogeneity,
275 and noise more generally, has on input-output response functions (Mejias & Longtin, 2014; Lefebvre et al.,
276 2015). This effect is illustrated in Figure 5(b). The bolded sigmoids represent the averaged activity of
277 the entire population of heterogeneous neurons alongside individual activation functions (fainter sigmoids).
278 Increased (resp. decreased) variability dampens (resp. sharpens) the averaged response curve for the non-
279 epileptogenic (resp. epileptogenic) setting. Such variability-induced linearization raises the excitability at

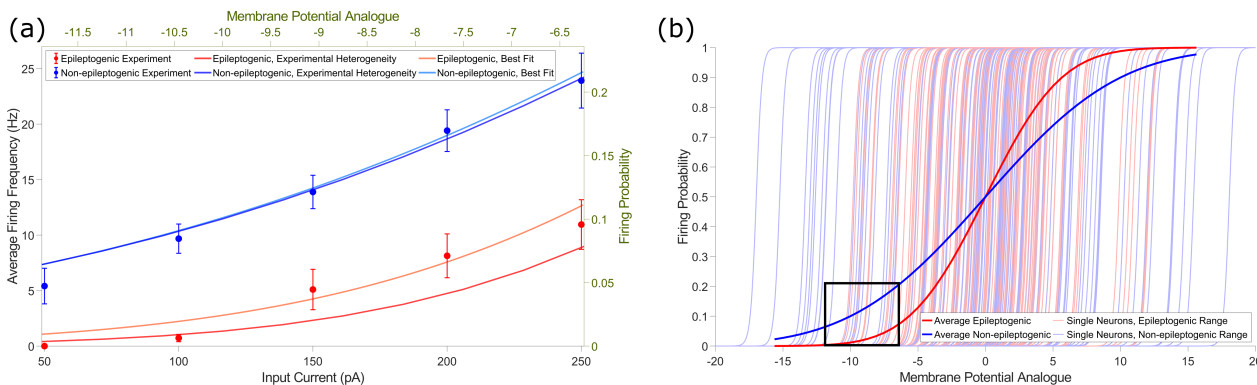


Figure 5. Differing levels of neuronal heterogeneity explain population activation function differences observed experimentally between epileptogenic and non-epileptogenic cortex. (a): Experimentally observed firing frequencies plotted against input current (left and bottom axes, mean \pm SEM) for epileptogenic frontal lobe (red) and non-epileptogenic MTG (blue) tissue (as shown previously in Figure 1(c)), visualized against an analogous measure of the relationship between population activity (firing probability) and drive (membrane potential analogue) in our neuron models (right and top axes, details in Methods). The shape of the curve for the heterogeneity value derived from epileptogenic tissue experimentally (red, $\sigma_e = 4.4$) qualitatively matches the experimental data, and a best fit (light red, $\sigma_e = 5.03$, $r^2=0.94$) is obtained with a similarly low heterogeneity value. In contrast, the curve associated with the heterogeneity value derived from non-epileptogenic tissue experimentally (blue, $\sigma_e = 7.8$) closely matches the experimental data from non-epileptogenic tissue and is nearly identical to the best fit (light blue, $\sigma_e = 7.77$, $r^2=0.98$). **(b):** A visualization of the entirety of the sigmoidal input-output relationship for our neuron models, with the regime compared to experimental data in panel (a) in a black box. Fainter curves represent input-output relationships for individual neurons, either epileptogenic (red) or non-epileptogenic (blue): the wider variability in the blue curves yields the flatter sigmoid representing the population activation function for our non-epileptogenic heterogeneity value, and vice-versa for the red curves associated with the epileptogenic heterogeneity value.

280 low input values, corresponding with the dynamics highlighted in Figure 5(a). Figure 5 illustrates that our
 281 model predicts significant differences in the activation function between epileptogenic and non-epileptogenic
 282 tissue, and that heterogeneity, or lack thereof, can explain counter-intuitive neuronal responses. However,
 283 these differences are not necessarily reflected in network dynamics, as illustrated by the similar network firing
 284 rates in Figure 4(a) and (c) at high levels of drive. In the context of seizure, this implies that excessive
 285 synchronization of a neural population need *not* be exclusively associated with increased excitability as
 286 represented by a lower firing threshold or higher firing rate of the population of isolated neurons.

287 Discussion

288 In this work, we propose that neuronal heterogeneity serves an important role in generating resilience to
 289 ictogenesis, and correspondingly that its loss may be a “final common pathway” for a number of etiologies
 290 associated with epilepsy. We explored this hypothesis using *in vitro* electrophysiological characterization of
 291 human cortical tissue from epileptogenic and non-epileptogenic areas, which revealed significant differences in
 292 DTT (a key determinant of neuronal excitability) heterogeneity in the pathological and non-pathological

293 settings. The ability to perform experiments on tissue from human subjects diagnosed with epilepsy makes
294 these results particularly relevant to the human condition. We then implemented these experimentally
295 observed heterogeneities in *in silico* spiking neural networks. Our explorations show that networks with high
296 heterogeneity, similar to the physiological setting, exhibit a more stable asynchronously firing state that is
297 resilient to sudden transitions into a more active and synchronous state. Differing heterogeneity levels also
298 explained the significant differences in the experimentally-obtained population activation functions between
299 epileptogenic and non-epileptogenic tissue. Finally, using mathematical analysis we show that differences in
300 the bifurcation structure of analogous mean-field systems provide a theoretical explanation for dynamical
301 differences in spiking networks. Viewed jointly, these three avenues of investigation provide strong evidence
302 that reduction in biophysical heterogeneity *exists* in epileptogenic tissue, can *yield dynamical changes* with
303 parallels to seizure onset, and that there are *theoretical principles* underlying these differences.

304 Computational studies have established the role played by heterogeneity in reducing synchronous activity
305 in the context of physiological gamma rhythms (Börgers & Kopell, 2003, 2005; Börgers et al., 2012). Other
306 investigations have implemented heterogeneity in more varied neural parameters (Yim et al., 2013) and
307 identified asymmetric effects of excitatory and inhibitory heterogeneities on network dynamics (Mejias &
308 Longtin, 2012, 2014). Our study complements and extends the understanding of the role of biophysical
309 heterogeneity in neural networks to human epilepsy by: 1) using experimentally derived heterogeneities of
310 the DTT in non-epileptogenic and epileptogenic surgical specimens, which when implemented *in silico* are
311 dynamically relevant; 2) exploring the effects of heterogeneity on the transition to synchrony, the hallmark of
312 seizure onset; 3) detailing the differing extents to which inhibitory and excitatory heterogeneity contribute
313 to circuit resilience to synchronous transitions. Our mathematical analysis further builds on this work to
314 provide a theoretical undergird for these observed dynamics.

315 The asymmetric effect of excitatory and inhibitory heterogeneities supports predictions regarding inhibitory
316 heterogeneity's role in ictogenesis. Supplementary Figure S2(a) shows that the sudden onset of synchrony
317 is more likely to arise for moderate values of σ_i than σ_e . The physiological heterogeneity of the entire
318 inhibitory population is likely to be larger than for the excitatory population (Cossart, 2011), driven in part
319 by the diverse subpopulations of interneurons (Huang & Paul, 2019). Thus, our work makes two interesting
320 predictions: first, a moderate loss of heterogeneity amongst inhibitory interneurons might be sufficient to make
321 a system vulnerable to ictogenesis; second, the preservation of inhibitory heterogeneity may provide a bulwark
322 against ictogenesis even if excitatory heterogeneity is pathologically reduced as observed experimentally. Of
323 note is that, in this work, changes in heterogeneity are “symmetric” (i.e., increased heterogeneity yields
324 a similar increase in both hyper- and hypo-active neurons). A subject of future investigation is whether
325 increasing the heterogeneity of the system “asymmetrically” (i.e., by only adding hyper- or hypo-active

326 neurons) would yield similar effects.

327 The loss of inhibitory cell types (Cobos et al., 2005; Cossart et al., 2001) or unique firing patterns of
328 inhibitory cells (Gavrilovici et al., 2012) previously shown to be associated with epilepsy can be thought of as
329 a loss of inhibitory heterogeneity. These studies tend to contextualize the epileptogenic effect of these changes
330 as driven by a deficit in GABAergic signalling, either due to the loss of inhibitory cells (Cobos et al., 2005) (or,
331 in the case of Cossart et al. (2001), the loss of specifically dendritic targeting inhibitory signaling) or to fewer
332 action potentials generated by inhibitory cells (Gavrilovici et al., 2012). We present a potential additional
333 route to the seizure state under such conditions, where the loss of inhibitory neuronal heterogeneity promotes
334 ictogenesis, which could serve to reconcile these studies' sometimes conflicting observations regarding the loss
335 of interneurons.

336 How might the decreased population excitability through homogenization of neuronal excitability we
337 observed be reconciled with the perspective of epilepsy as a disorder of hyper-excitability? Our findings
338 suggest that within the epileptogenic zone, interictal hypometabolism (Niu et al., 2021) and manifestations
339 of “hyper-excitability,” such as inter-ictally recorded high-frequency oscillations (HFOs) and inter-ictal
340 spikes (IIDs) (Frauscher et al., 2017; Jiruska et al., 2017), can coexist. In essence, our findings suggest
341 that the observed hypometabolism may arise in part from cellular homogenization that reduces population
342 excitability (see Figure 1(c) and 5(b)) - since metabolism is tightly linked to maintaining ionic gradients
343 and thus firing rates - while simultaneously facilitating the emergence of synchronous activities (Figure 4(c))
344 such as HFOs, IIDs and seizures. In addition, our work also hints at a process of “disinhibition through
345 neural homogenization” - decreased population excitability in inhibitory populations through homogenization,
346 together with our observation that sudden transitions occurred for more moderate values of σ_i , indicates
347 suppression in overall inhibition. Such disinhibition may further explain the hypometabolism observed
348 interictally given that interneuronal spiking appears to contribute more to brain metabolism than pyramidal
349 cells (Ackermann et al., 1984). While conjectural, further studies using targeted patching of interneurons in
350 both human and chronic rodent models are warranted to answer these questions, and characterize what, if
351 any, homogenization occurs in interneuronal populations during epileptogenesis and epilepsy.

352 While our results include lower neuronal counts from the frontal lobe, this represents a less common
353 source of human cortical tissue than non-epileptogenic MTG. For this reason, we use the population of
354 non-epileptogenic frontal lobe neurons (obtained during tumor resection) only as evidence that heterogeneity
355 levels are not confounded by comparison between the temporal and frontal lobes, and limit our modeling
356 work to comparing non-epileptogenic MTG and epileptogenic frontal lobe. The factor limiting the sample size
357 of epileptogenic neurons was the necessity to confirm the epileptogenicity of the resected cortex using
358 electrocorticography (ECoG), making this data set highly selective. Although one might obtain a greater

359 sample by comparing non-epileptogenic MTG to epileptogenic mesial temporal structures (i.e., subiculum,
360 parahippocampal gyrus, hippocampus) this would represent comparison between the allocortex and neocortex
361 which would add a further confound. Alternatively, obtaining non-epileptogenic medial temporal lobe
362 (MTL) cortex is exceedingly rare. With these important limitations in the access to human cortical tissue
363 considered, our comparison between epileptogenic frontal lobe, non-epileptogenic (tumor) frontal lobe, and
364 non-epileptogenic MTG represent a best-case comparison of the biophysical properties of epileptogenic and
365 non-epileptogenic human tissue while reasonably controlling for confounds introduced by the differing brain
366 regions, and our computational and mathematical explorations using this data maximize the conclusions that
367 can be drawn despite the limitations imposed by the human setting.

368 Our model networks, while analogous to E-I microcircuits commonly used in computational investigations
369 of cortical activity (Renart et al., 2010; Ostojic, 2014; Vogels & Abbott, 2009), are simplified from the
370 biophysical reality and must be considered with these limitations in mind; indeed, such models cannot
371 reasonably capture the full richness and complexity of seizure dynamics and do not include multiple inhibitory
372 populations (Huang & Paul, 2019). However, this simplifying choice facilitates findings that have their
373 foundation in fundamental mathematical principles and are not especially reliant on biophysical intricacies
374 such as network topology (see the confirmation of the robustness of our models in Supplementary Figures
375 S6 and S7). This increases the likelihood that these predictions are generalizable. Potential future work
376 involves the use of more biophysically detailed human inspired neuron and network models, allowing for
377 the implementation and study of additional types of heterogeneity (including multiple, diverse inhibitory
378 populations) and/or the study of model seizures. Such studies will be facilitated by our recent development
379 of a biophysically-detailed computational model of a human L5 cortical pyramidal neuron (Rich et al., 2021),
380 allowing them to be more directly applicable to potential clinical applications for the treatment of human
381 epilepsy. In this vein, while we do not model seizures per se in this work, the two most common types of seizure
382 onsets observed in intracranial recordings are the low-voltage fast (Lee et al., 2000) and hyper-synchronous
383 onsets (Velascol et al., 1999). Both reflect a sudden transition from a desynchronized state to a synchronous
384 oscillation, albeit of differing frequencies. Given the ubiquity of such onsets, our modeling of the transition to
385 synchrony is likely to be broadly relevant to epilepsy.

386 Lastly, one might wonder what neurobiological processes render an epileptogenic neuronal population less
387 biophysically diverse. While under physiological conditions channel densities are regulated within neurons to
388 obtain target electrical behaviors (Marder, 2011), it remains speculative as to what processes might lead to
389 pathological homogenization of neuronal populations. However, modeling suggests that biological diversity
390 may be a function of input diversity, and thus “homogenizing the input received by a population of neurons
391 should lead the population to be less diverse” (Tripathy et al., 2013). Although requiring further exploration,

392 it is possible that the information-poor, synchronous post-synaptic barrages accompanying seizure (Trevelyan
393 et al., 2013) represent such a homogenized input, reducing a circuit's resilience to synchronous transitions
394 and promoting epileptogenesis by reducing biophysical heterogeneity.

395 **Acknowledgments**

396 We thank Frances Skinner, Shreejoy Tripathy, Prajay Shah, and Anukrati Nigam for productive intellectual
397 discussions on this topic in the project's early stages. We thank the National Sciences and Engineering
398 Research Council of Canada (NSERC Grants RGPIN-2017-06662 to J.L. and RGPIN-2015-05936 to T.A.V.),
399 the Krembil Foundation (Krembil Seed Grant to J.L. and T.A.V.), the University of Toronto Department
400 of Physiology (Yuet Ngor Wong Award to S.R.), and the Savoy Foundation (Steriade-Savoy Postdoctoral
401 Fellowship to S.R.) for support of this research.

402 **Author Contributions**

403 Conception and design: SR, HMC, JL, TAV. Experimental data collection: HMC. Data analysis and
404 interpretation: SR, HMC, TAV. Simulations: SR. Mathematical analysis: SR, JL. Initial drafting: SR. Edits
405 and revisions: SR, HMC, JL, TAV. All authors approved the version to be submitted.

406 **Competing Interests**

407 The authors have declared that no conflict of interest exists.

408 **Materials and Methods**

409 **Experiment: Human brain slice preparation**

410 All procedures on human tissue were performed in accordance with the Declaration of Helsinki and approved
411 by the University Health Network Research Ethics board. Patients underwent a standardized temporal or
412 frontal lobectomy (Fallah et al., 2012) under general anesthesia using volatile anesthetics for seizure treatment
413 (Beaulieu-Laroche et al., 2018). Tissue was obtained from patients diagnosed with temporal or frontal lobe
414 epilepsy who provided written consent. Tissue from temporal lobe was obtained from 22 patients, age ranging
415 between 21 to 63 years (mean age \pm SEM: 37.8 ± 2.9). The resected temporal lobe tissue displayed no
416 structural or functional abnormalities in preoperative MRI and was deemed "healthy" tissue considering it is

417 located outside of the epileptogenic zone. Tissue from frontal lobe was obtained from five patients, age ranging
418 between 23-36 years (mean age \pm SEM: 30.2 ± 2.4), and was deemed “epileptogenic” tissue as confirmed
419 using electrocorticography (ECoG), making this data set highly selective. Tissue from non-epileptogenic
420 frontal lobe obtained during tumor resection was obtained from two patients, ages 37 and 58 years, and was
421 also considered “non-epileptogenic”.

422 After surgical resection, the cortical tissue block was instantaneously submerged in ice-cold ($\sim 4^{\circ}\text{C}$) cutting
423 solution that was continuously bubbled with 95% O_2 -5% CO_2 containing (in mM): sucrose 248, KCl 2,
424 $\text{MgSO}_4 \cdot 7\text{H}_2\text{O}$ 3, $\text{CaCl}_2 \cdot 2\text{H}_2\text{O}$ 1, NaHCO_3 26, $\text{NaH}_2\text{PO}_4 \cdot \text{H}_2\text{O}$ 1.25, and D-glucose 10. The osmolarity was
425 adjusted to 300-305 mOsm. The human tissue samples were transported (5-10 min) from Toronto Western
426 Hospital (TWH) to the laboratory for further slice processing. Transverse brain slices ($400 \mu\text{m}$) were obtained
427 using a vibratome (Leica 1200 V) perpendicular to the pial surface to ensure that pyramidal cell dendrites were
428 minimally truncated (Beaulieu-Laroche et al., 2018; Kalmbach et al., 2018) in the same cutting solution as
429 used for transport. The total duration, including slicing and transportation, was kept to a maximum of 20-30
430 minutes. After sectioning, the slices were incubated for 30 min at 34°C in standard artificial cerebrospinal
431 fluid (aCSF) (in mM): NaCl 123, KCl 4, $\text{CaCl}_2 \cdot 2\text{H}_2\text{O}$ 1, $\text{MgSO}_4 \cdot 7\text{H}_2\text{O}$ 1, NaHCO_3 26, $\text{NaH}_2\text{PO}_4 \cdot \text{H}_2\text{O}$ 1.2,
432 and D-glucose 10. The pH was 7.40 and after incubation the slice was held for at least for 60 min at room
433 temperature. aCSF in both incubation and recording chambers were continuously bubbled with carbogen gas
434 (95% O_2 -5% CO_2) and had an osmolarity of 300-305 mOsm.

435 **Experiment: Electrophysiological recordings and intrinsic physiology feature** 436 **analysis**

437 Slices were transferred to a recording chamber mounted on a fixed-stage upright microscope (Axioskop 2
438 FS MOT; Carl Zeiss, Germany). Recordings were performed from the soma of pyramidal neurons at 32 - 34°
439 in recording aCSF continually perfused at 4 ml/min. Cortical neurons were visualized using an IR-CCD
440 camera (IR-1000, MTI, USA) with a 40x water immersion objective lens. Using the IR-DIC microscope, the
441 boundary between layer 1 (L1) and 2 (L2) was easily distinguishable in terms of cell density. Below L2, the
442 sparser area of neurons (L3) was followed by a tight band of densely packed layer 4 (L4) neurons, with a
443 decrease in cell density indicating layer 5 (L5) (Moradi Chameh et al., 2021; Kalmbach et al., 2021).

444 Patch pipettes (3-6 $\text{M}\Omega$ resistance) were pulled from standard borosilicate glass pipettes (thin-wall
445 borosilicate tubes with filaments, World Precision Instruments, Sarasota, FL, USA) using a vertical puller
446 (PC-10, Narishige). Pipettes were filled with intracellular solution containing (in mM): K-gluconate 135;
447 NaCl 10; HEPES 10; MgCl_2 1; Na_2ATP 2; GTP 0.3, pH adjusted with KOH to 7.4 (290–309 mOsm).

448 Whole-cell patch-clamp recordings were obtained using a Multiclamp 700A amplifier, Axopatch 200B
449 amplifier, pClamp 9.2 and pClamp 10.6 data acquisition software (Axon instruments, Molecular Devices,
450 USA). Electrical signals were digitized at 20 kHz using a 1320X digitizer. The access resistance was monitored
451 throughout the recording (typically between 8-25 M Ω), and neurons were discarded if the access resistance
452 was >25 M Ω . The liquid junction potential was calculated to be -10.8 mV and was not corrected.

453 Electrophysiological data were analyzed off-line using Clampfit 10.7, Python and MATLAB (MATLAB,
454 2019). Electrophysiological features were calculated from responses elicited by 600 ms square current steps
455 as previously described (Moradi Chameh et al., 2021). Briefly, the resting membrane potential (RMP) was
456 measured after breaking into the cell (IC=0). The firing threshold was determined following depolarizing
457 current injections between 50 to 250 pA with 50 pA step size for 600 ms; the threshold was calculated by finding
458 the voltage value corresponding with a value of $\frac{dV}{dt}$ that was 5% of the average maximal $\frac{dV}{dt}$ across all action
459 potentials elicited by the input current that first yielded action potential firing. The distance to threshold
460 presented in this paper was calculated as the difference between the RMP and threshold. The average FI curve
461 (i.e., activation function) was generated by calculating the instantaneous frequency at each spike for each of
462 the depolarizing current injections (50-250 pA, step size 50 pA, 600 ms) and averaging over the population.
463 Spike frequency adaptation ratio was calculated from the first current injection that yielded at least four
464 spikes, and is defined as the mean of the ratio of subsequent inter-spike intervals. This could not be quantified
465 in every neuron if sufficient spiking was not elicited by the current-clamp protocol. This analysis utilizes the
466 IPFX package made available through the Allen Institute (<https://github.com/AllenInstitute/ipfx>),
467 as used by Berg et al. (2021) amongst others.

468 Plotting of experimental data was performed using GraphPad Prism 6 (GraphPad software, Inc, CA,
469 USA). The non-parametric Mann-Whitney test was used to determine statistical differences between the
470 means of two groups. The F-test was used to compare standard deviation (SD) between groups. The two
471 sample coefficient of variation test was used to compare the coefficient of variance (CV) between groups.
472 Normality of the data was tested with the Shapiro-Wilk and D'Agostino & Pearson omnibus normality tests
473 with alpha=0.05. The one-way ANOVA post hoc with Dunn's multiple comparison test was used to determine
474 statistical significance in the spike frequency adaptation ratio. A standard threshold of p<0.05 is used to
475 report statistically significant differences.

476 **Modeling: spiking neural network**

477 The cortical spiking neural network contains populations of recurrently connected excitatory and inhibitory
478 neurons (Snyder & Miller, 2012; Stevens & Zador, 1996). The spiking response of those neurons obeys the

479 non-homogeneous Poisson process

$$Y_j \rightarrow \text{Poisson}(f(u_j, h_j)) \quad (1)$$

480 where $Y_j = \sum_l \delta(t - t_k)$ is a Poisson spike train with rate $f(u_j, h_j)$.

481 The firing rate of neuron j is determined by the non-linear sigmoidal activation function $f(u_j, h_j)$,

$$f(u_j, h_j) = \frac{1}{1 + e^{-\beta(u_j - h_j)}} \quad (2)$$

482 where u_j is the membrane potential analogue and h_j represents the rheobase. The constant $\beta = 4.8$ scales
483 the non-linear gain.

484 Heterogeneity is implemented via the rheobases h_j . The h_j values are chosen by independently and
485 randomly sampling a normal Gaussian distribution whose standard deviation is $\sigma_{e,i}$ if neuron j is excitatory
486 (e) or inhibitory (i). The values of σ_i and σ_e are varied throughout these explorations between a minimum
487 value of 2.5 mV and a maximum value of 16.75 mV. The heterogeneity parameters for the model have a direct
488 parallel with the heterogeneity in the distance to threshold (DTT) measured experimentally, with β chosen
489 so that the experimentally observed heterogeneity values and the heterogeneity parameters implemented in
490 the model are within the same range (compare Figure 1(b) and Figure 2(c-d)).

491 The membrane potential analogue u_j is defined by

$$\frac{du_j}{dt} = \alpha_x (-u_j(t) + \text{Syn}_j^{ex} + \text{Syn}_j^{ix} + I_x + I(t)) + \sqrt{2\alpha_x}DX_j \quad (3)$$

492 The variable α_x represents the time constant depending upon whether the neuron j is excitatory ($x = e, \alpha_e = 10$
493 ms) or inhibitory ($x = i, \alpha_i = 5$ ms). The differential time scales are implemented given the different membrane
494 time constants between cortical pyramidal neurons and parvalbumin positive (PV) interneurons (Neske et al.,
495 2015).

496 Syn_j^{ex} and Syn_j^{ix} are the synaptic inputs to the cell j (from the excitatory and inhibitory populations,
497 respectively), dependent upon whether cell j is excitatory ($x = e$) or inhibitory ($x = i$). Our cortical model
498 is built of 800 excitatory and 200 inhibitory neurons (Traub et al., 1997; Rich et al., 2017, 2018). The
499 connectivity density for each connection type (E-E, E-I, I-E, and I-I) is varied uniformly via a parameter p .
500 In this study, $p = 1$ is used (i.e., all-to-all connectivity) with the exception of in Supplementary Figure S5.
501 The synaptic strengths are represented by w_{xy} where $x, y = e, i$ depending upon whether the pre-synaptic cell
502 (x) and the post-synaptic cell (y) are excitatory or inhibitory. In our model, $w_{ee} = 100.000$, $w_{ei} = 187.500$,
503 $w_{ie} = -293.750$, and $w_{ii} = -8.125$. Negative signs represent inhibitory signalling, while positive signs
504 represent excitatory signalling. These values are chosen to place the network near a tipping point between

505 asynchronous and synchronous firing based on mathematical analysis and previous modeling work (Rich
506 et al., 2020b), and scaled relative to the values of β .

507 The post-synaptic inputs Syn_j^{ex} and Syn_j^{ix} are given by

$$Syn_j^{ex} = \frac{1}{800} \sum_{k=1, k \neq j}^{800} c_{kj} \frac{w_{ex}}{p} Y_k(t - \Delta t) \quad (4)$$

508

$$Syn_j^{ix} = \frac{1}{200} \sum_{k=1, k \neq j}^{200} c_{kj} \frac{w_{ix}}{p} Y_k(t - \Delta t) \quad (5)$$

509 where $x = e, i$ and Y_k is a Poisson spike train given by $Y_k = \sum_l \delta(t - t_l)$. The connectivity scheme excludes
510 auto-synapses. c_{kj} represents the connectivity: if neuron k synapses onto neuron j , $c_{kj} = 1$, and otherwise
511 $c_{kj} = 0$. The synaptic weights are scaled by the connectivity density p so that the net input signal to each
512 neuron is not affected by the number of connections.

513 Equation 3 includes three non-synaptic inputs to the neuron: I_x , $I(t)$, and $\sqrt{2\alpha_x D}X_j$. The variable
514 X_j is a spatially independent Gaussian white noise process. The value of noise intensity was chosen so that
515 the noise-induced fluctuations are commensurate with endogenous dynamics of the network. I_x represents a
516 bias current whose value depends on whether the neuron is excitatory ($x = e$) or inhibitory ($x = i$), imparting
517 a differential baseline spiking rate to these distinct populations. Here, $I_i = -31.250$, ensuring that inhibitory
518 neurons will typically require excitatory input to fire, matching biophysical intuition. $I_e = -15.625$ is based
519 on previous literature (Jadi & Sejnowski, 2014a,b; Neske et al., 2015; Rich et al., 2020b) to position the
520 system near the transition between asynchronous and synchronous firing.

521 $I(t)$ implements time-varying external input only applied to the excitatory population (this is simply
522 referred to as the “drive” to the system in Figures 2, 3 and 4). In this work, this term is used primarily
523 to study the response of the spiking network to a linear ramp excitatory input that occurs at a time scale
524 much slower than the dynamics of individual neurons: to yield the ramp current used throughout the study
525 $I(t)$ simply varies linearly between 0 and 31.25 over a 2500 ms simulation (for computational efficiency, the
526 simulation length is limited to 2048 ms for the heatmaps displayed in Supplementary Figures S2 and S5).
527 In Supplementary Figure S2(b), where we characterize the dynamics of the network with constant input,
528 $I(t) = 15.625$ uniformly.

529 The final probability of a Poisson neuron j firing at time t depends upon the effect of these various
530 elements on u_j :

$$\rho_j = 1 - e^{-f(u_j(t), h_j)dt} \quad (6)$$

531 Parameter values

532 Parameter values summarized in Table 1 below are analogous to those used in previous work on oscillatory
533 cortical networks (Jadi & Sejnowski, 2014a,b; Neske et al., 2015; Rich et al., 2020b) with the scaling of our
534 chosen β accounted for.

Table 1. Key model parameters.

Parameter	Value
Number of excitatory neurons	800
Number of inhibitory neurons	200
Excitatory time constant, α_e	10 ms
Inhibitory time constant, α_i	5 ms
Non-linear gain of activation function, β	4.8
Variance of noisy input, D	3.906
Excitatory bias current, I_e	-15.625
Inhibitory bias current, I_i	-31.250
External input, $I(t)$	Variable
Excitatory-excitatory synaptic strength, w_{ee}	100.000
Excitatory-inhibitory synaptic strength, w_{ei}	187.500
Inhibitory-inhibitory synaptic strength, w_{ii}	-8.125
Inhibitory-excitatory synaptic strength, w_{ie}	-293.750
Excitatory heterogeneity, σ_e	Variable
Inhibitory heterogeneity, σ_i	Variable
rheobase, h	Variable
Connectivity density, p	Variable
Time step, Δt	1 ms

535 Numerics

536 All sampling from standard normal Gaussian distributions is done via the Box-Mueller algorithm (Golder &
537 Settle, 1976). Equations are integrated using the Euler-Maruyama method. In our simulations, $\Delta t = 0.1$,
538 scaled so that each time step Δt represents 1 ms.

539 The excitatory network synchrony (i.e. Synchrony Measure) and excitatory and inhibitory firing rates are
540 calculated over sliding 100 ms time windows in Figures 2, 3 and 4. To preserve symmetry and ensure initial
541 transients do not skew the data, our first window begins at $t = 100$.

542 The Synchrony Measure is an adaptation of a commonly used measure developed by Golomb and Rinzel
543 (Golomb & Rinzel, 1993, 1994) to quantify the degree of coincident spiking in a network as utilized in our
544 previous studies (Rich et al., 2016, 2017, 2018, 2020a). Briefly, the measure involves convolving a very narrow
545 Gaussian function with the time of each action potential for every cell to generate functions $V_i(t)$. The
546 population averaged voltage $V(t)$ is then defined as $V(t) = \frac{1}{N} \sum_{i=1}^N V_i(t)$, where N is the number of cells in the
547 network. The overall variance of the population averaged voltage $\text{Var}(V)$ and the variance of an individual

548 neuron's voltage $\text{Var}(V_i)$ is defined as

$$\text{Var}(V) = \langle V(t)^2 \rangle - \langle V(t) \rangle^2 \quad (7)$$

549 and

$$\text{Var}(V_i) = \langle V_i(t)^2 \rangle - \langle V_i(t) \rangle^2 \quad (8)$$

550 where $\langle \cdot \rangle$ indicates time averaging over the interval for which the measure is taken. The Synchrony
551 Measure S is then defined as

$$S = \frac{\text{Var}(V)}{\frac{1}{N} \sum_{i=1}^N \text{Var}(V_i)} \quad (9)$$

552 The value $S = 0$ indicates completely asynchronous firing, while $S = 1$ corresponds to fully synchronous
553 network activity. Intermediate values represent intermediate degrees of synchronous firing.

554 In the case of sliding time bins, this measure is taken by only considering spikes falling into the time
555 window of interest. In Figure 4 we present averages of S over 100 independent realizations, and if a particular
556 run yields a “NaN” result for S at a given time step (indicating no spikes in the associated window), we
557 eliminate that value from the average for that time point (this increases the variability of these values since
558 there are less to average over; thus, this is reflected in an increased range of the \pm STD curves). In contrast,
559 in Supplementary Figure S2**(b)** we generate a single value the Synchrony Measure (or the other measures of
560 interest) over the last 1000 ms of the simulation. Supplementary Figure S2**(b)** displays this measure averaged
561 over five independent simulations.

562 Supplementary Figure S2 includes the presentation of our Bifurcation Measure B . This quantifies the
563 presence of sudden and significant changes in the Synchrony Measure over time. First, we take the Synchrony
564 Measure time series for each independent run (i.e., as presented in Figure 3), and use the *smooth* function in
565 MATLAB (MATLAB, 2019) with a 500 step window, generating a new time series from this moving average
566 filter. This low-pass filter serves to account for fluctuations arising when, for example, a particular 100
567 ms window includes more or less activity than average. We denote this filtered time-series S_s . Second, we
568 calculate the difference quotient $\frac{\delta S_s}{\delta I}$, where I is the value of the external drive (plotted against time in
569 Figure 3), at each step in the time series. Finally, we take the variance of the values of $\frac{\delta S_s}{\delta I}$ using the *var*
570 function in MATLAB (MATLAB, 2019): networks in which the Synchrony Measure changes in a consistently
571 linear fashion will have a tight distribution of $\frac{\delta S_s}{\delta I}$ around the average slope (see, for example, Figure 3**(b)**),
572 and thus a low variance; in contrast, networks in which the Synchrony Measure undergoes abrupt transitions

573 will yield a multi-modal distribution of $\frac{\delta S_s}{\delta I}$, with each mode corresponding to different linear sections of S_s ,
574 and thus the variance of these values will be notably higher (see, for example, Figure 3(c)). The plotted
575 value of B represents an average over the B values calculated for each independent network instantiation.
576 We note that when we calculate the “firing rate Bifurcation Measure” B_e in reference to the four scenarios
577 in Figure 4, we simply replicate the above steps on the firing rate time series rather than the Synchrony
578 Measure time series.

579 We emphasize that the Bifurcation Measure is appropriate for identifying the dynamics of interest in
580 this work given that the related quantifications increase largely monotonically in response to increased drive,
581 especially once these time series are “smoothed” prior to the application of this measure. The smoothed
582 Synchrony Measure and firing rates do not display any discontinuous behaviors in our experimental paradigms
583 that might confound this measure.

584 Analysis of FI curves

585 In Figure 5, we compare activation functions derived from experimental data with model analogues (i.e., the
586 function F described below in Equation 12). In Figure 5(b) we show examples of F with epileptogenic and
587 non-epileptogenic levels of heterogeneity alongside samples of the function f (Equation 2) randomly chosen
588 based on the differing heterogeneity levels.

589 In Figure 5(a), we confirm the correspondence between the F functions and the experimental data by
590 determining the value of σ_e best fitting this data. This process involved three steps: first, we qualitatively
591 determined the portion of the F curves most likely to fit this data as that in $-11.875 \leq U_e \leq -6.25$; second,
592 both the x (U_e , [-11.875 -6.25]) and y (probability of firing, [0.003585 .2118]) variables were re-scaled to match
593 the ranges exhibited by the x (input current, pA, [50 250]) and y (firing frequency, Hz, [0 24]) variables in the
594 experimental data; finally, a fit was calculated using MATLAB’s (MATLAB, 2019) Curve Fitting application.
595 This process used a non-linear least squares method, with $r^2 > .93$ for both fits (see details in Results).
596 Additional scaling was performed for plotting so that the two x- and y-axes in Figure 5 remain consistent.

597 Modeling: Mean-field reduction

598 Following previous work (Hutt et al., 2016; Stefanescu et al., 2012; Hutt et al., 2020; Rich et al., 2020b;
599 Lefebvre et al., 2015; Hutt et al., 2020) we perform a mean-field reduction of the spiking network in Equation
600 3. We assume that the firing rate of cells is sufficiently high to make use of the diffusion approximation

601 (Gluss, 1967), yielding

$$\alpha_e^{-1} \frac{dU_e}{dt} = -U_e + w_{ee}F(U_e, \sigma_e) + w_{ie}F(U_i, \sigma_i) + I^e \quad (10)$$

$$\alpha_i^{-1} \frac{dU_i}{dt} = -U_i + w_{ii}F(U_i, \sigma_i) + w_{ei}F(U_e, \sigma_i) + I^i \quad (11)$$

602 where $U_{e,i} = \sum_{j=1}^{N_{e,i}} w_{e,i}^j$ represents the mean activity of the excitatory or inhibitory population, respectively.

603 The function F represents the average activation function conditioned upon the value of $\sigma_{e,i}$ via the
604 convolution

$$F(U_{e,i}, \sigma_{e,i}) = \int_{-\infty}^{\infty} f(U_{e,i} + v, 0) \rho(v, \sigma_{e,i}) dv \quad (12)$$

605 where $\rho(v, \sigma_{e,i}) = N(0, \sigma_{e,i}^2)$ (Lefebvre et al., 2015; Hutt et al., 2018, 2016).

606 Linear stability analysis of the mean-field equations

607 Fixed points $\bar{U}_{e,i}$ of the mean-field equations satisfy

$$0 = -\bar{U}_e + w_{ee}F(\bar{U}_e, \sigma_e) + w_{ie}F(\bar{U}_i, \sigma_i) + I^e \quad (13)$$

$$0 = -\bar{U}_i + w_{ii}F(\bar{U}_i, \sigma_i) + w_{ei}F(\bar{U}_e, \sigma_e) + I^i \quad (14)$$

608 Linearizing about the steady state values of $\bar{U}_{e,i}$ yields the system

$$\mathbf{A} \begin{pmatrix} \delta \bar{U}_e \\ \delta \bar{U}_i \end{pmatrix} = \begin{pmatrix} -1 + w_{ee}\alpha_e R^e & w_{ie}\alpha_i R^i \\ w_{ei}\alpha_e R^e & -1 + w_{ii}\alpha_i R^i \end{pmatrix} \begin{pmatrix} \delta \bar{U}_e \\ \delta \bar{U}_i \end{pmatrix} \quad (15)$$

609 with $R^{e,i} = R(\bar{U}_e, \bar{U}_i) = \int_{\Omega(v)} f'[\bar{U}_{e,i} + v, 0] \rho(v, \sigma_{e,i}) dv$. The system's stability is given by the eigenvalues of
610 the Jacobian \mathbf{A} . Define

$$B = \text{trace}(\mathbf{A}) = -(-2 + (w_{ee}\alpha_e) R^e + (w_{ii}\alpha_i) R^i) \quad (16)$$

$$C = \det(\mathbf{A}) = (-1 + (w_{ee}\alpha_e) R^e) (-1 + (w_{ii}\alpha_i) R^i) - ((w_{ie}\alpha_i) R^i) ((w_{ei}\alpha_e) R^e) \quad (17)$$

611 Eigenvalues of \mathbf{A} are thus given by

$$\lambda_{\pm} = \frac{-B \pm \sqrt{B^2 - 4C}}{2} \quad (18)$$

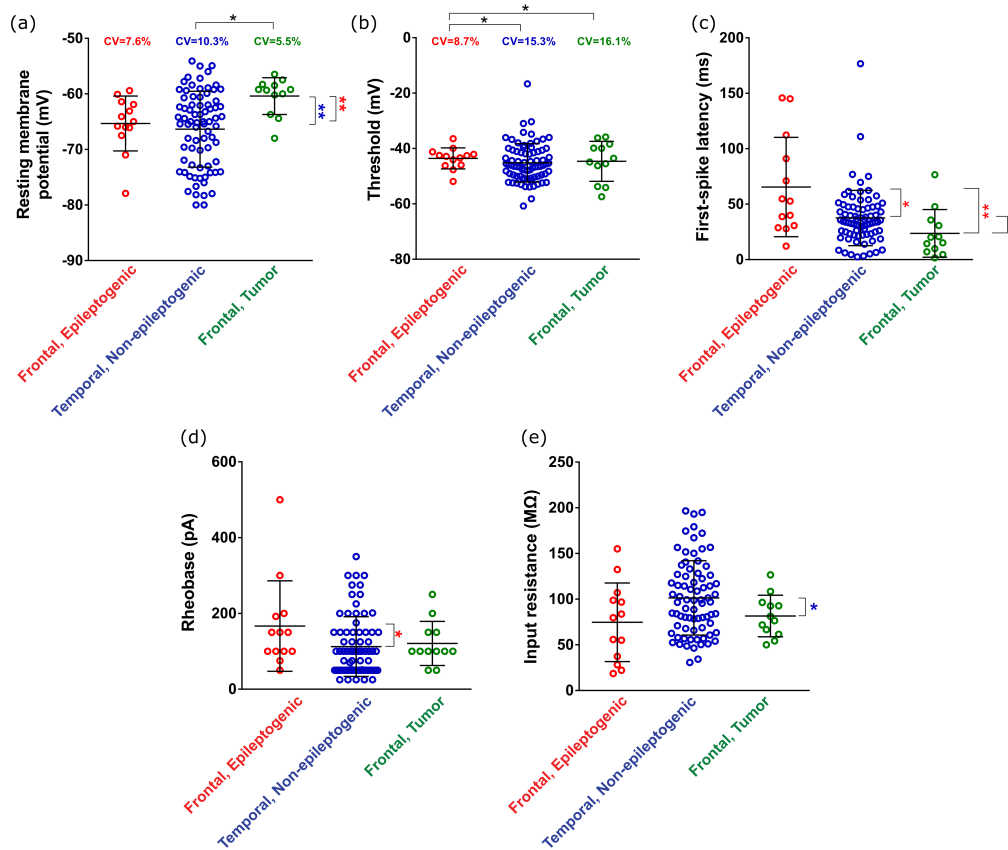
612 **Bifurcation analysis with varying excitatory input**

613 We investigate bifurcation properties as a function of I^e . In Supplementary Figure S2(a), multi-stability, as
614 denoted by the bold border, is determined by testing for the presence of multiple fixed points at I^e ranging
615 from -15.625:0.625:-6.250, a range encompassing the range for multi-stability shown in Figure 4 (noting
616 $I^e = I_e + I(t)$).

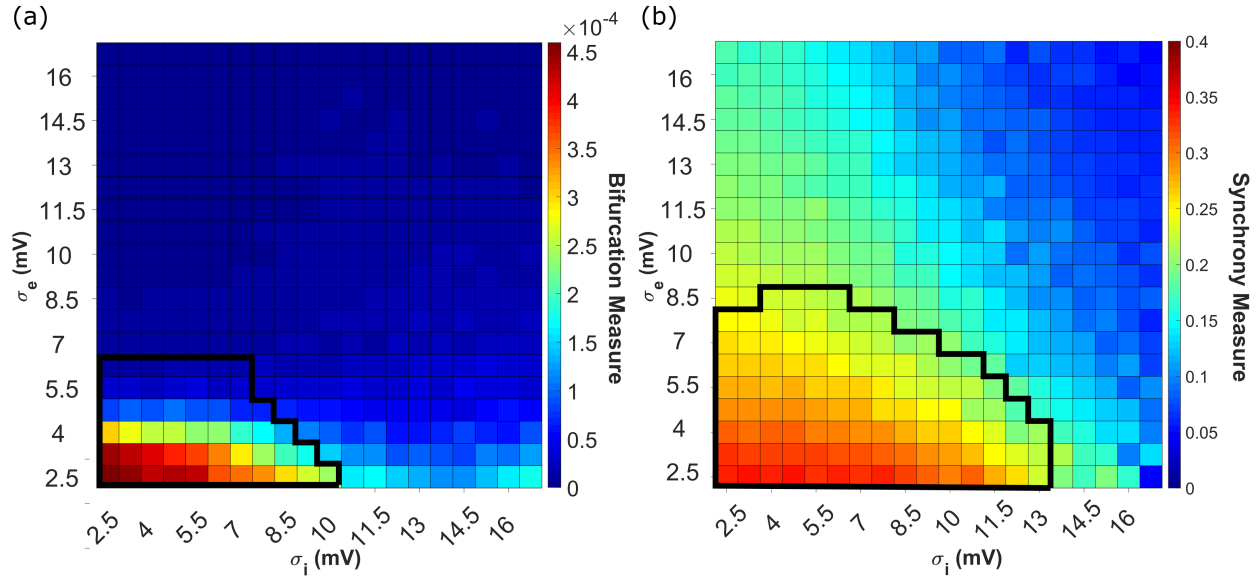
617 **Code Accessibility**

618 The code generating the primary figures is available at <https://github.com/Valiantelab/LostNeuralHeterogeneity>.
619 Additional code used is available upon request to the authors.

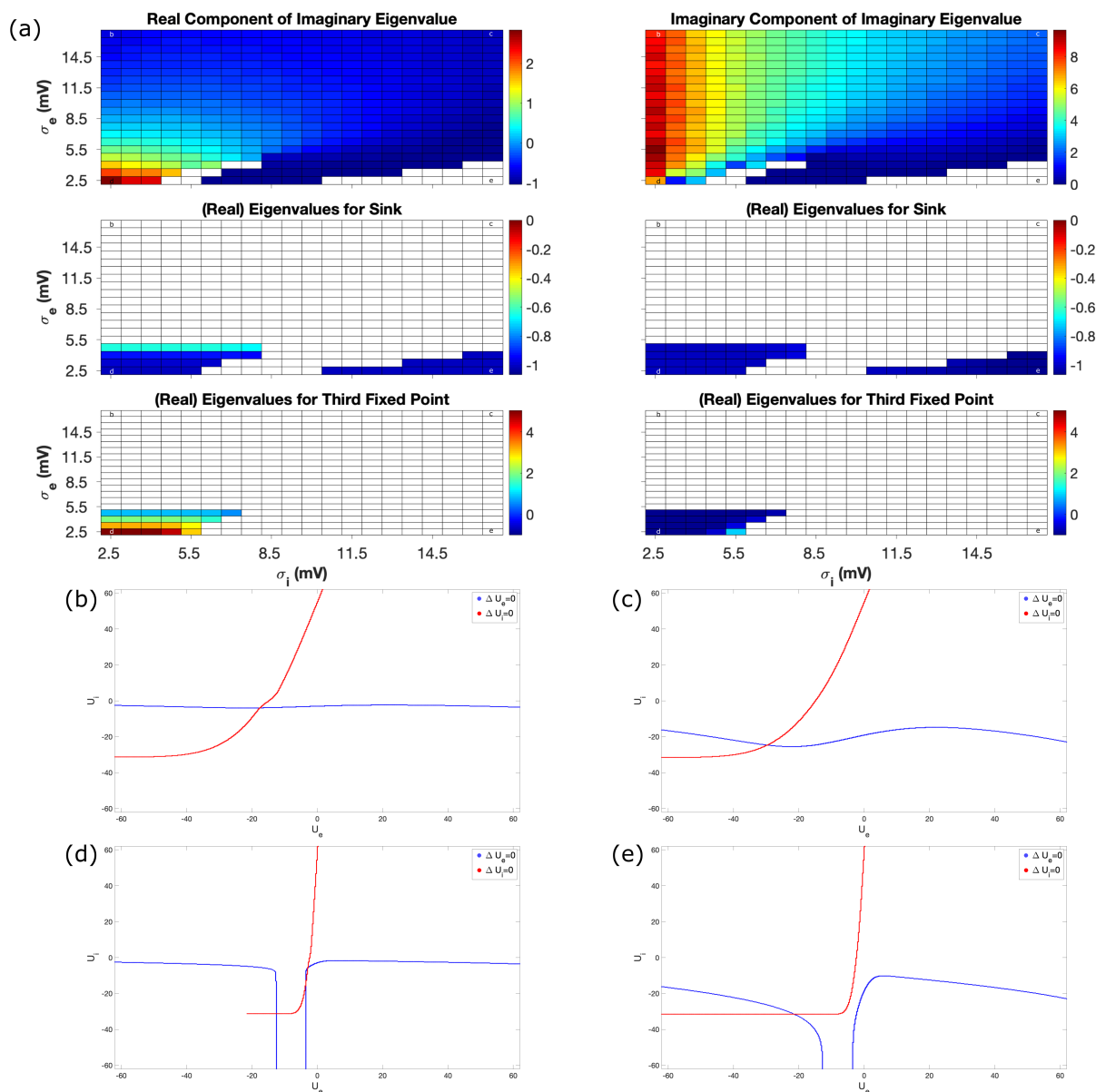
620 **Supplementary Figures**



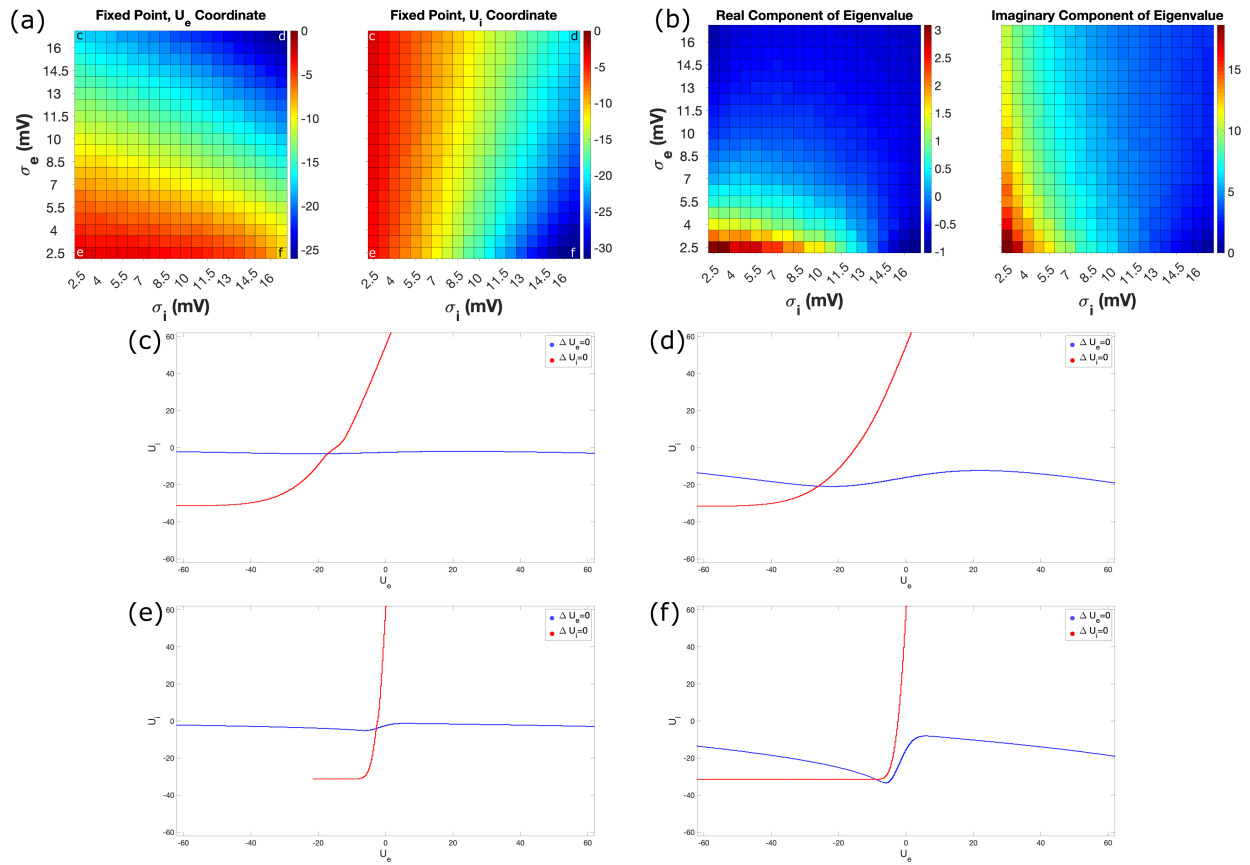
Supplementary Figure S1. Details from electrophysiological recordings. (a): Distribution of resting membrane potentials (RMP) in our three neuronal populations. None of the distributions are deemed normal after failing the D’Agostino and Pearson omnibus, Shapiro-Wilk, and Kolmogorof-Smirnov normality tests with $\alpha=0.05$. Mean RMP is significantly increased in the frontal, tumor ($n=12$) population compared to both the frontal, epileptogenic ($n=13$; $p=0.003$; Non-parametric Mann-Whitney test) and temporal, non-epileptogenic ($n=77$; $p=0.002$) populations. Coefficient of variation (CV) of these populations is significantly increased in the temporal, non-epileptogenic population compared to the frontal, tumor population ($p=0.03$; two sample coefficient of variation test). Plotted bars indicate mean \pm standard deviation (SD). (b): Distribution of threshold voltages in our three neuronal populations. All three distributions are deemed normal after passing the Kolmogorof-Smirnov normality test with $\alpha=0.05$. No significant differences between mean threshold voltages were observed (unpaired t test with Welch’s correction). The CV of the threshold voltage in the frontal, epileptogenic population was significantly lower than in the temporal, non-epileptogenic population ($p=0.04$) and than in the frontal, tumor population ($p=0.04$). Plotted bars indicate mean \pm SD. (c) Distribution of first-spike latencies (time between stimulus application and first spike) in our three neuronal populations. None of the distributions are deemed normal. Mean latency is significantly lower in the temporal, non-epileptogenic population compared to the frontal, epileptogenic population ($p=0.03$; Non-parametric Mann-Whitney test), and mean latency is significantly lower in the frontal, tumor population compared to both the frontal, epileptogenic ($p=0.0045$) and temporal, non-epileptogenic ($p=0.02$) populations. Plotted bars indicate mean \pm SD. (d) Distribution of rheobases (minimal input current required to elicit first spike) in our three neuronal populations. None of the distributions are deemed normal. The mean rheobase of the temporal, non-epileptogenic population is significantly lower compared to the frontal, epileptogenic population ($p=0.045$; Non-parametric Mann-Whitney test). Plotted bars indicate mean \pm SD. (e) Distribution of input resistances in our three neuronal populations. All three distributions are deemed normal after passing the D’Agostino and Pearson omnibus, Shapiro-Wilk, and Kolmogorof-Smirnov normality tests with $\alpha=0.05$. Mean input resistance of the frontal, tumor population is significantly lower compared to the temporal, non-epileptogenic population ($p=0.02$; Unpaired t-test with Welch’s correction). Plotted bars indicate mean \pm SD.



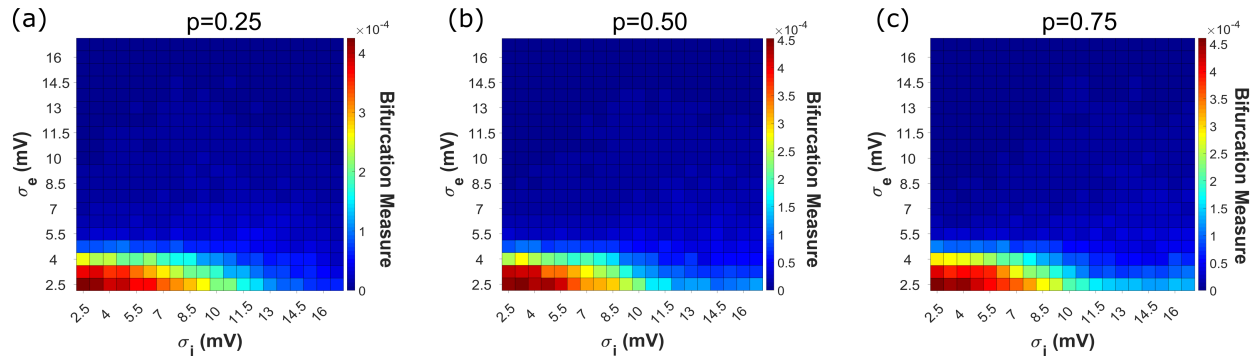
Supplementary Figure S2. Exploration of a larger σ_e and σ_i parameter space highlights the asymmetric effects of excitatory and inhibitory heterogeneity on sudden transitions into synchrony. (a): Visualization quantifying the tendency for spiking networks to undergo a sudden and notable increase in excitatory synchrony over time, when subjected to a linearly increasing input as in Figures 2, 3, and 4 (but over 2048 as opposed to 2500 ms), via the Bifurcation Measure B . Results are shown averaged over 10 independent simulations. Bolded region demarcates networks whose mean-field analogues exhibit any multi-stability from those that do not (remainder of heatmap). (b): Dynamics of spiking networks with a constant external input ($I(t) = 15.625$) where either synchronous or asynchronous activity can arise. The excitatory synchrony is quantified via the Synchrony Measure taken over the final 1000 ms of a 2048 ms simulation, and the presented value is averaged over five independent simulations. The bolded region demarcates networks whose mean-field analogues have an unstable oscillator from those that have a stable oscillator (remainder of heatmap) as their lone fixed point when $I(t) = 15.625$.



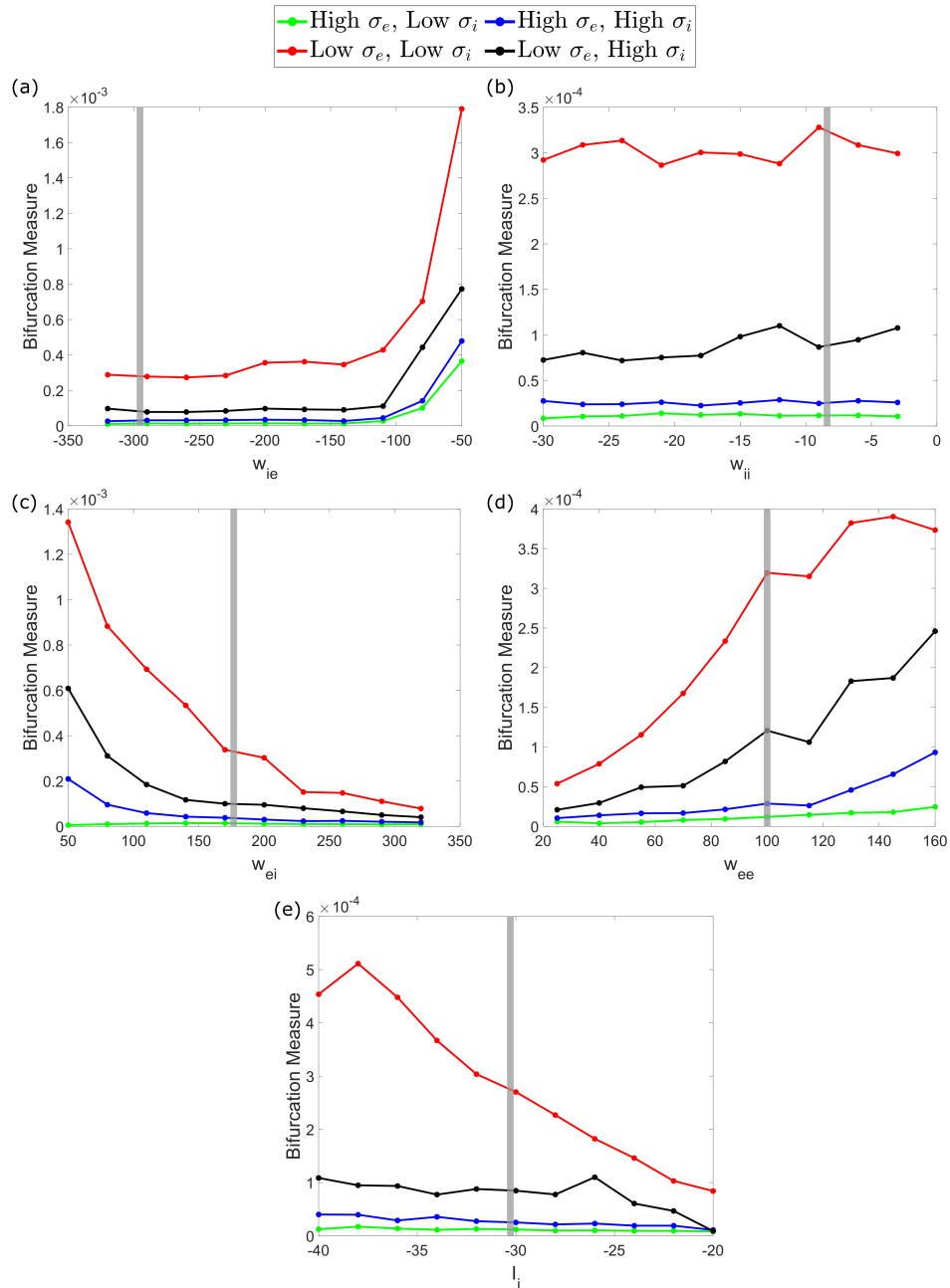
Supplementary Figure S3. Fixed points and eigenvalues of mean-field equations for $I(t) = 3.125$. (a): The mean-field system with this $I(t)$ value can yield multiple fixed points: we calculate their eigenvalues, sort them by their classifications, and visualize these eigenvalues via heatmaps. In this example, we see that multiple fixed points arise only when both σ_e and σ_i are low (i.e. the bottom-left of the heatmap). (b-e): Fixed points are determined by finding the intersections of the U_e and U_i nullclines, visualized for the corners of our heatmap (top-left in panel (b), top-right in panel (c), bottom-left in panel (d), and bottom-right in panel (e)). Multiple fixed points correspond with multiple intersections of these curves, as seen exclusively in panel (d).



Supplementary Figure S4. Fixed points and eigenvalues of mean-field equations for $I(t) = 15.625$. (a): As all mean-field systems in our parameter space yield a single fixed point when $I(t) = 15.625$, we visualize the U_e and U_i coordinates of this fixed point using a heatmap. (b): Each fixed point has imaginary eigenvalues, which we visualize by plotting the real and imaginary components of the eigenvalue associated with the fixed point in a heatmap. (c-f): Fixed points are determined by finding the intersections of the U_e and U_i nullclines, visualized for the corners of our heatmap (top-left in panel (c), top-right in panel (d), bottom-left in panel (e), and bottom-right in panel (f)).



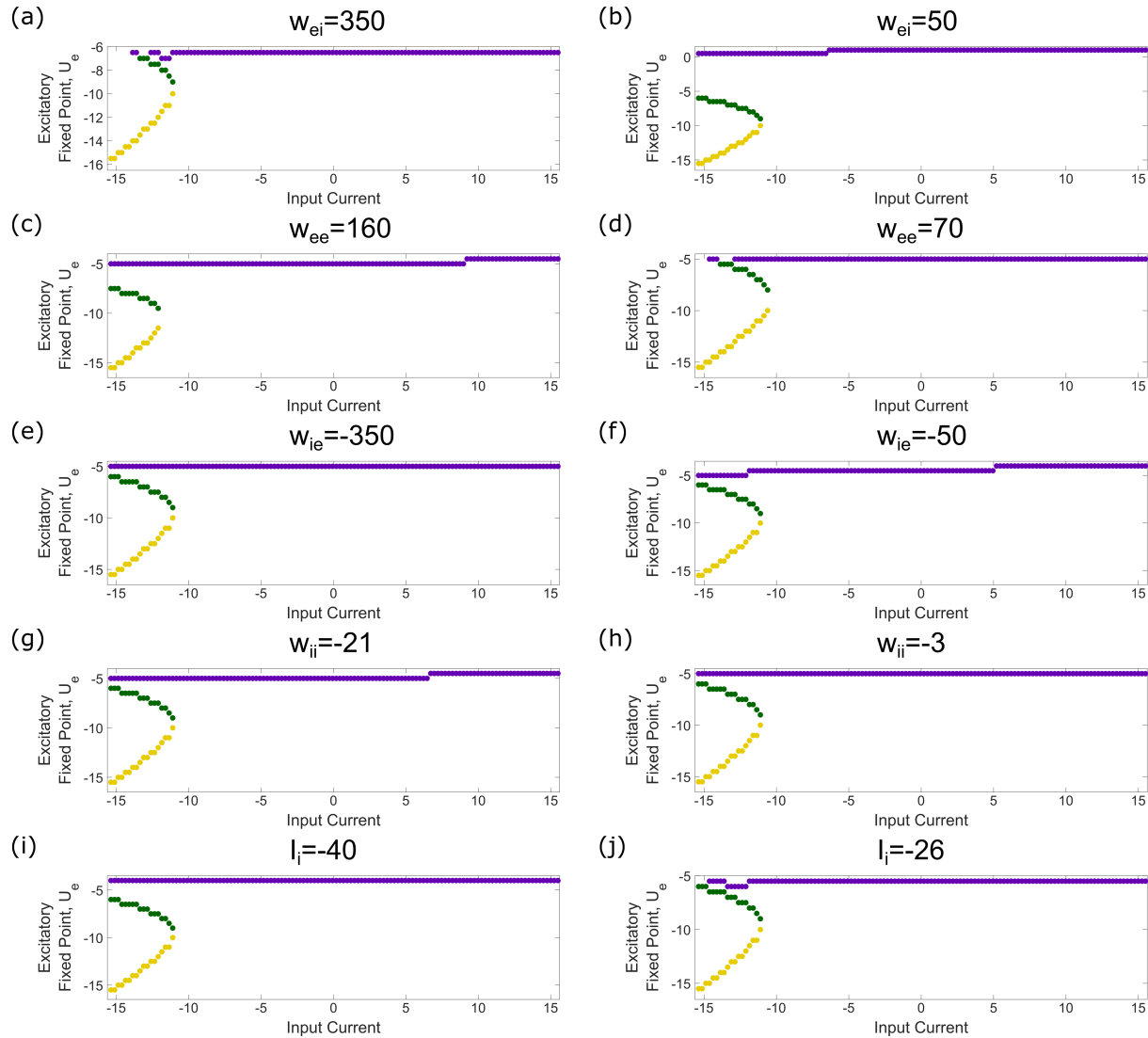
Supplementary Figure S5. Dynamics of spiking networks are robust to more sparse connectivity paradigms. Bifurcation Measure B pattern over our parameter space remains similar with $p = 0.25$ (panel (a)), $p = 0.50$ (panel (b)), and $p = 0.75$ (panel (c)), when compared to the case of $p = 1.00$ seen in Figure S2(a). In each case the “asymmetry” in the effects of σ_e and σ_i is preserved. Heatmaps present results averaged over ten independent simulations.



Supplementary Figure S6. Network dynamics are robust to a range of parameters. (a-d):

Examination of changes to network dynamics, as quantified via the Bifurcation Measure, caused by varying a single synaptic weight (w_{ie} in (a), w_{ii} in (b), w_{ei} in (c), and w_{ee} in (d)) or the baseline inhibitory drive (I_i in (e)).

Vertical grey bar represents the default value as given in Table 1. Values of high/low heterogeneity correspond with those used in exemplar networks in Figures 3 and 4. The Bifurcation Measure is always highest when both σ_e and σ_i are low (red trace), and the other traces (each representing a scenario where at least one of σ_e and σ_i is high) rarely exceed the default Bifurcation Measure of the low σ_e and σ_i case (approximately 3×10^{-4}). This indicates “sudden transitions” into synchronous dynamics on the magnitude of that seen in Figure 3(c) and Figure 4(c) occur preferentially in the case of both low σ_e and σ_i , even for variations of these parameters. The preserved relationship between the four scenarios represented by the different traces (low σ_e and low σ_i always yielding the highest bifurcation measure, followed by low σ_e and high σ_i , followed then by very similar values in both high σ_e scenarios) is further evidence of the robustness of the patterns observed in the results of Figures 3 and 4. Each data point represents an average over 10 independent simulations.



Supplementary Figure S7. Bifurcation structures are robust to a range of parameters. To confirm the robustness of our spiking network dynamics implies similar robustness in our mean-field systems, we performed bifurcation analyses similar to those in Figure 4 (but with less numerical precision due to computational constraints). Similarly to Supplementary Figure S6 we varied the parameters individually, and showcase examples at high and low extremes for each parameter that clearly preserve the unique bifurcation structure seen in Figure 4(c). This is done for w_{ei} in (a-b), w_{ee} in (c-d), w_{ie} in (e-f), w_{ii} in (g-h), and I_i in (i-j).

621 **References**

- 622 Ackermann, R. F., Finch, D. M., Babb, T. L., & Engel, J. (1984). Increased glucose metabolism during
623 long-duration recurrent inhibition of hippocampal pyramidal cells. *Journal of Neuroscience*, 4, 251–264.
- 624 Albertson, A. J., Yang, J., & Hablitz, J. J. (2011). Decreased hyperpolarization-activated currents in layer
625 5 pyramidal neurons enhances excitability in focal cortical dysplasia. *Journal of neurophysiology*, 106,
626 2189–2200.
- 627 Altschuler, S. J. & Wu, L. F. (2010). Cellular heterogeneity: do differences make a difference? *Cell*, 141,
628 559–563.
- 629 Arnold, E. C., McMurray, C., Gray, R., & Johnston, D. (2019). Epilepsy-induced reduction in hcn channel
630 expression contributes to an increased excitability in dorsal, but not ventral, hippocampal ca1 neurons.
631 *Eneuro*, 6.
- 632 Beaulieu-Laroche, L., Toloza, E. H., van der Goes, M.-S., Lafourcade, M., Barnagian, D., Williams, Z. M., Es-
633 kandar, E. N., Frosch, M. P., Cash, S. S., & Harnett, M. T. (2018). Enhanced dendritic compartmentalization
634 in human cortical neurons. *Cell*, 175, 643–651.
- 635 Berg, J., Sorensen, S. A., Ting, J. T., Miller, J. A., Chartrand, T., Buchin, A., Bakken, T. E., Budzillo,
636 A., Dee, N., Ding, S.-L., et al. (2021). Human neocortical expansion involves glutamatergic neuron
637 diversification. *Nature*, 598, 151–158.
- 638 Boland, R. P., Galla, T., & McKane, A. J. (2008). How limit cycles and quasi-cycles are related in systems
639 with intrinsic noise. *Journal of Statistical Mechanics: Theory and Experiment*, 2008, P09001.
- 640 Börgers, C., Franzesi, G. T., LeBeau, F. E., Boyden, E. S., & Kopell, N. J. (2012). Minimal size of cell
641 assemblies coordinated by gamma oscillations. *PLoS Comput Biol*, 8, e1002362.
- 642 Börgers, C. & Kopell, N. (2003). Synchronization in networks of excitatory and inhibitory neurons with
643 sparse, random connectivity. *Neural computation*, 15, 509–538.
- 644 Börgers, C. & Kopell, N. (2005). Effects of noisy drive on rhythms in networks of excitatory and inhibitory
645 neurons. *Neural computation*, 17, 557–608.
- 646 Chow, S.-N. & Hale, J. K. (2012). *Methods of bifurcation theory*, vol. 251. (Springer Science & Business
647 Media).

- 648 Cobos, I., Calcagnotto, M. E., Vilaythong, A. J., Thwin, M. T., Noebels, J. L., Baraban, S. C., & Rubenstein,
649 J. L. (2005). Mice lacking *dlx1* show subtype-specific loss of interneurons, reduced inhibition and epilepsy.
650 *Nature neuroscience*, 8, 1059–1068.
- 651 Colder, B. W., Frysinger, R. C., Wilson, C. L., Harper, R. M., & Engel Jr, J. (1996). Decreased neuronal
652 burst discharge near site of seizure onset in epileptic human temporal lobes. *Epilepsia*, 37, 113–121.
- 653 Cossart, R. (2011). The maturation of cortical interneuron diversity: how multiple developmental journeys
654 shape the emergence of proper network function. *Current opinion in neurobiology*, 21, 160–168.
- 655 Cossart, R., Dinocourt, C., Hirsch, J., Merchan-Perez, A., De Felipe, J., Ben-Ari, Y., Esclapez, M., & Bernard,
656 C. (2001). Dendritic but not somatic gabaergic inhibition is decreased in experimental epilepsy. *Nature*
657 *neuroscience*, 4, 52–62.
- 658 Dehghani, N., Peyrache, A., Telenczuk, B., Le Van Quyen, M., Halgren, E., Cash, S. S., Hatsopoulos, N. G.,
659 & Destexhe, A. (2016). Dynamic balance of excitation and inhibition in human and monkey neocortex.
660 *Scientific reports*, 6, 1–12.
- 661 Fallah, A., Akl, E. A., Ebrahim, S., Ibrahim, G. M., Mansouri, A., Foote, C. J., Zhang, Y., & Fehlings,
662 M. G. (2012). Anterior cervical discectomy with arthroplasty versus arthrodesis for single-level cervical
663 spondylosis: a systematic review and meta-analysis. *PLoS One*, 7, e43407.
- 664 Frauscher, B., Bartolomei, F., Kobayashi, K., Cimbalnik, J., van 't Klooster, M. A., Rampp, S., Otsubo, H.,
665 Höller, Y., Wu, J. Y., Asano, E., et al. (2017). High-frequency oscillations: the state of clinical research.
666 *Epilepsia*, 58, 1316–1329.
- 667 Gavrilovici, C., Pollock, E., Everest, M., & Poulter, M. O. (2012). The loss of interneuron functional diversity
668 in the piriform cortex after induction of experimental epilepsy. *Neurobiology of disease*, 48, 317–328.
- 669 Gluss, B. (1967). A model for neuron firing with exponential decay of potential resulting in diffusion equations
670 for probability density. *Bulletin of Mathematical Biophysics*, 29, 233–243.
- 671 Golder, E. & Settle, J. (1976). The box-müller method for generating pseudo-random normal deviates.
672 *Journal of the Royal Statistical Society: Series C (Applied Statistics)*, 25, 12–20.
- 673 Golomb, D. & Rinzel, J. (1993). Dynamics of globally coupled inhibitory neurons with heterogeneity. *Physical*
674 *review E*, 48, 4810.
- 675 Golomb, D. & Rinzel, J. (1994). Clustering in globally coupled inhibitory neurons. *Physica D: Nonlinear*
676 *Phenomena*, 72, 259–282.

- 677 Hodge, R. D., Bakken, T. E., Miller, J. A., Smith, K. A., Barkan, E. R., Graybuck, L. T., Close, J. L., Long,
678 B., Johansen, N., Penn, O., et al. (2019). Conserved cell types with divergent features in human versus
679 mouse cortex. *Nature*, 573, 61–68.
- 680 Huang, Z. J. & Paul, A. (2019). The diversity of gabaergic neurons and neural communication elements.
681 *Nature Reviews Neuroscience*, 20, 563–572.
- 682 Hutt, A., Lefebvre, J., Hight, D., & Kaiser, H. A. (2020). Phase coherence induced by additive gaussian and
683 non-gaussian noise in excitable networks with application to burst suppression-like brain signals. *Frontiers*
684 *in applied mathematics and statistics*, 5, 69.
- 685 Hutt, A., Lefebvre, J., Hight, D., & Sleight, J. (2018). Suppression of underlying neuronal fluctuations
686 mediates EEG slowing during general anaesthesia. *Neuroimage*, 179, 414–428.
- 687 Hutt, A., Mierau, A., & Lefebvre, J. (2016). Dynamic control of synchronous activity in networks of spiking
688 neurons. *PloS one*, 11.
- 689 Jadi, M. P. & Sejnowski, T. J. (2014a). Cortical oscillations arise from contextual interactions that regulate
690 sparse coding. *Proceedings of the National Academy of Sciences*, 111, 6780–6785.
- 691 Jadi, M. P. & Sejnowski, T. J. (2014b). Regulating cortical oscillations in an inhibition-stabilized network.
692 *Proceedings of the IEEE*, 102, 830–842.
- 693 Jasper, H. H. (2012). *Jasper’s basic mechanisms of the epilepsies*, vol. 80. (OUP USA).
- 694 Jirsa, V. K., Stacey, W. C., Quilichini, P. P., Ivanov, A. I., & Bernard, C. (2014). On the nature of seizure
695 dynamics. *Brain*, 137, 2210–2230.
- 696 Jiruska, P., Alvarado-Rojas, C., Schevon, C. A., Staba, R., Stacey, W., Wendling, F., & Avoli, M. (2017).
697 Update on the mechanisms and roles of high-frequency oscillations in seizures and epileptic disorders.
698 *Epilepsia*, 58, 1330–1339.
- 699 Jiruska, P., De Curtis, M., Jefferys, J. G., Schevon, C. A., Schiff, S. J., & Schindler, K. (2013). Synchronization
700 and desynchronization in epilepsy: controversies and hypotheses. *The Journal of physiology*, 591, 787–797.
- 701 Kalmbach, B. E., Buchin, A., Long, B., Close, J., Nandi, A., Miller, J. A., Bakken, T. E., Hodge, R. D.,
702 Chong, P., de Frates, R., et al. (2018). h-channels contribute to divergent intrinsic membrane properties of
703 supragranular pyramidal neurons in human versus mouse cerebral cortex. *Neuron*, 100, 1194–1208.

- 704 Kalmbach, B. E., Hodge, R. D., Jorstad, N. L., Owen, S., de Frates, R., Yanny, A. M., Dalley, R., Mallory,
705 M., Graybuck, L. T., Radaelli, C., et al. (2021). Signature morpho-electric, transcriptomic, and dendritic
706 properties of human layer 5 neocortical pyramidal neurons. *Neuron*, 109, 2914–2927.
- 707 Klaassen, A., Glykys, J., Maguire, J., Labarca, C., Mody, I., & Boulter, J. (2006). Seizures and enhanced
708 cortical gabaergic inhibition in two mouse models of human autosomal dominant nocturnal frontal lobe
709 epilepsy. *PNAS*, 103, 19152–19157.
- 710 Kramer, M. A., Kirsch, H. E., & Szeri, A. J. (2005). Pathological pattern formation and cortical propagation
711 of epileptic seizures. *Journal of the Royal Society Interface*, 2, 113–127.
- 712 Lee, S.-A., Spencer, D. D., & Spencer, S. S. (2000). Intracranial eeg seizure-onset patterns in neocortical
713 epilepsy. *Epilepsia*, 41, 297–307.
- 714 Lefebvre, J., Hutt, A., Knebel, J.-F., Whittingstall, K., & Murray, M. M. (2015). Stimulus statistics shape
715 oscillations in nonlinear recurrent neural networks. *Journal of Neuroscience*, 35, 2895–2903.
- 716 Marder, E. (2011). Variability, compensation, and modulation in neurons and circuits. *Proceedings of the*
717 *National Academy of Sciences of the United States of America*, 108 Suppl 3, 15542–15548.
- 718 Marder, E. & Goaillard, J.-M. (2006). Variability, compensation and homeostasis in neuron and network
719 function. *Nature Reviews Neuroscience*, 7, 563.
- 720 MATLAB (2019). version 9.6.0 (R2019a). (Natick, Massachusetts: The MathWorks Inc.).
- 721 Mejias, J. & Longtin, A. (2012). Optimal heterogeneity for coding in spiking neural networks. *Physical*
722 *Review Letters*, 108, 228102.
- 723 Mejias, J. F. & Longtin, A. (2014). Differential effects of excitatory and inhibitory heterogeneity on the gain
724 and asynchronous state of sparse cortical networks. *Frontiers in computational neuroscience*, 8, 107.
- 725 Mishra, P. & Narayanan, R. (2019). Disparate forms of heterogeneities and interactions among them drive
726 channel decorrelation in the dentate gyrus: Degeneracy and dominance. *Hippocampus*, 29, 378–403.
- 727 Moradi Chameh, H., Rich, S., Wang, L., Chen, F.-D., Zhang, L., Carlen, P. L., Tripathy, S. J., & Valiante,
728 T. A. (2021). Diversity amongst human cortical pyramidal neurons revealed via their sag currents and
729 frequency preferences. *Nature Communications*, 12.
- 730 Neske, G. T., Patrick, S. L., & Connors, B. W. (2015). Contributions of diverse excitatory and inhibitory
731 neurons to recurrent network activity in cerebral cortex. *Journal of Neuroscience*, 35, 1089–1105.

- 732 Niu, N., Xing, H., Wu, M., Ma, Y., Liu, Y., Ba, J., Zhu, S., Li, F., & Huo, L. (2021). Performance of pet
733 imaging for the localization of epileptogenic zone in patients with epilepsy: a meta-analysis. *European*
734 *Radiology*, 31, 1–14.
- 735 Ostojic, S. (2014). Two types of asynchronous activity in networks of excitatory and inhibitory spiking
736 neurons. *Nature neuroscience*, 17, 594–600.
- 737 Padmanabhan, K. & Urban, N. N. (2010). Intrinsic biophysical diversity decorrelates neuronal firing while
738 increasing information content. *Nature neuroscience*, 13, 1276.
- 739 Renart, A., De La Rocha, J., Bartho, P., Hollender, L., Parga, N., Reyes, A., & Harris, K. D. (2010). The
740 asynchronous state in cortical circuits. *Science*, 327, 587–590.
- 741 Reynolds, E. H. (2002). Introduction: epilepsy in the world. *Epilepsia*, 43, 1–3.
- 742 Rich, S., Booth, V., & Zochowski, M. (2016). Intrinsic cellular properties and connectivity density determine
743 variable clustering patterns in randomly connected inhibitory neural networks. *Frontiers in neural circuits*,
744 10, 82.
- 745 Rich, S., Chameh, H. M., Rafiee, M., Ferguson, K. A., Skinner, F. K., & Valiente, T. A. (2020a). Inhibitory
746 network bistability explains increased interneuronal activity prior to seizure onset. *Frontiers in Neural*
747 *Circuits*, 13, 81.
- 748 Rich, S., Hutt, A., Skinner, F. K., Valiante, T. A., & Lefebvre, J. (2020b). Neurostimulation stabilizes spiking
749 neural networks by disrupting seizure-like oscillatory transitions. *Scientific reports*, 10, 1–17.
- 750 Rich, S., Moradi Chameh, H., Sekulic, V., Valiante, T. A., & Skinner, F. K. (2021). Modeling reveals
751 human–rodent differences in h-current kinetics influencing resonance in cortical layer 5 neurons. *Cerebral*
752 *Cortex*, 31, 845–872.
- 753 Rich, S., Zochowski, M., & Booth, V. (2017). Dichotomous dynamics in ei networks with strongly and weakly
754 intra-connected inhibitory neurons. *Frontiers in neural circuits*, 11, 104.
- 755 Rich, S., Zochowski, M., & Booth, V. (2018). Effects of neuromodulation on excitatory–inhibitory neural
756 network dynamics depend on network connectivity structure. *Journal of Nonlinear Science*, 30, 1–24.
- 757 Saggio, M. L., Crisp, D., Scott, J. M., Karoly, P., Kuhlmann, L., Nakatani, M., Murai, T., Dumpelmann, M.,
758 Schulze-Bonhage, A., Ikeda, A., Cook, M., Gliske, S. V., Lin, J., Bernard, C., Jirsa, V., & Stacey, W. C.
759 (2020). A taxonomy of seizure dynamotypes. *Elife*, 9, e55632.

- 760 Savov, V. & Todorov, G. (2000). On a method for determining limit cycles in nonlinear circuits. *International*
761 *journal of electronics*, 87, 827–840.
- 762 Schwartzkroin, P. A., Turner, D. A., Knowles, W. D., & Wyler, A. R. (1983). Studies of human and monkey
763 “epileptic” neocortex in the in vitro slice preparation. *Annals of Neurology: Official Journal of the American*
764 *Neurological Association and the Child Neurology Society*, 13, 249–257.
- 765 Snyder, D. L. & Miller, M. I. (2012). *Random point processes in time and space*. (Springer Science & Business
766 Media).
- 767 Stefanescu, R. A., Shivakeshavan, R., & Talathi, S. S. (2012). Computational models of epilepsy. *Seizure*, 21,
768 748–759.
- 769 Stevens, C. F. & Zador, A. M. (1996). When is an integrate-and-fire neuron like a poisson neuron? In
770 *Advances in neural information processing systems*, pp. 103–109.
- 771 Sutula, T. P. & Dudek, F. E. (2007). Unmasking recurrent excitation generated by mossy fiber sprouting in
772 the epileptic dentate gyrus: an emergent property of a complex system. *Progress in brain research*, 163,
773 541–563.
- 774 Traub, R. D., Jefferys, J. G., & Whittington, M. A. (1997). Simulation of gamma rhythms in networks of
775 interneurons and pyramidal cells. *Journal of computational neuroscience*, 4, 141–150.
- 776 Trevelyan, A. J., Bruns, W., Mann, E. O., Crepel, V., & Scanziani, M. (2013). The information content of
777 physiological and epileptic brain activity. *The Journal of physiology*, 591, 799–805.
- 778 Tripathy, S. J., Padmanabhan, K., Gerkin, R. C., & Urban, N. N. (2013). Intermediate intrinsic diversity
779 enhances neural population coding. *Proceedings of the National Academy of Sciences*, 110, 8248–8253.
- 780 Velascol, A. L., Wilson, C. L., Babb, T. L., & Engel Jr, J. (1999). Functional and anatomic correlates of two
781 frequently observed temporal lobe seizure-onset patterns. *Neural plasticity*, 7, 49–63.
- 782 Vogels, T. P. & Abbott, L. (2009). Gating multiple signals through detailed balance of excitation and
783 inhibition in spiking networks. *Nature neuroscience*, 12, 483.
- 784 Yim, M. Y., Aertsen, A., & Rotter, S. (2013). Impact of intrinsic biophysical diversity on the activity of
785 spiking neurons. *Physical Review E*, 87, 032710.
- 786 Zhang, Z., Valiante, T., & Carlen, P. (2011). Transition to seizure: from “macro”-to “micro”-mysteries.
787 *Epilepsy research*, 97, 290–299.

788 Žiburkus, J., Cressman, J. R., & Schiff, S. J. (2013). Seizures as imbalanced up states: excitatory and
789 inhibitory conductances during seizure-like events. *Journal of neurophysiology*, 109, 1296–1306.